Geoscientific
Model Development
Discussions

Impacts of a double-moment bulk cloud microphysics scheme (NDW6-G23) on aerosol fields in NICAM.19 with a global 14-km grid resolution

Daisuke Goto[1], Tatsuya Seiki[2], Kentaroh Suzuki[3], Hisashi Yashiro[1], Toshihiko Takemura[4]

5

[1]National Institute for Environmental Studies, Tsukuba, 305-8506, Japan
[2]Japan Agency for Marine-Earth Science and Technology, Yokohama, 236-0001, Japan
[3]Atmosphere and Ocean Research Institute, The University of Tokyo, Kashiwa, 277-8568, Japan
[4]Research Institute for Applied Mechanics, Kyushu University, Fukuoka, 816-8580, Japan

10

Correspondence to: Daisuke Goto (goto.daisuke@nies.go.jp)

Abstract. In accordance with progression in current capabilities towards high-resolution approaches, applying a convective-permitting resolution to global aerosol models helps comprehend how complex cloud-precipitation systems interact with aerosols. This study investigates the impacts of a double-moment bulk cloud microphysics scheme, i.e., NICAM Double-

15 moment bulk Water 6 developed in this study (NDW6-G23), on the spatiotemporal distribution of aerosols in the Non-hydrostatic Icosahedral Atmospheric Model as part of the version 19 series (NICAM.19) with 14 km grid spacing. The mass concentrations and optical thickness of the NICAM-simulated aerosols are generally comparable to those obtained from in situ measurements, but some aerosol species, especially dust and sulfate, have larger differences among the experiments with NDW6 and NSW6 compared to those among the experiments with different horizontal resolutions, i.e., 14 km and 56 km grid

20 spacing, as shown in a previous study. The simulated aerosol burdens using NDW6 are generally lower than those using NSW6; the instantaneous radiative forcing due to aerosol-radiation interaction (IRFari) is estimated to be -1.57 Wm^{-2} (NDW6) and -1.86 Wm^{-2} (NSW6) in the global annual mean values of shortwave all-aerosol radiative forcing at the top of the atmosphere (TOA). This difference among the experiments using different cloud microphysics modules, e.g., 0.29 Wm^{-2} or 16% difference in IRFari values, is attributed to a different ratio of column precipitation to the sum of the column precipitation

25 and column liquid cloud water, which strongly determines the magnitude of wet deposition in the simulated aerosols. Since the simulated ratios in the NDW6 experiment are larger than those of the NSW6 result, the scavenging effect of the simulated aerosols in the NDW6 experiment is larger than that in the NSW6 experiment. A large difference between the experiments is also found in the aerosol indirect effect (AIE), i.e., the shortwave effective radiative forcing due to aerosol-cloud interaction (ERFaci) from the present to preindustrial days, which is estimated to be -1.34 Wm^{-2} (NDW6) and -0.63 Wm^{-2} (NSW6) in

30 global annual mean values. The magnitude of the ERFaci value in the NDW6 experiment is larger than that in the NSW6 result, probably due to the differences in the susceptibility of the simulated cloud water to the simulated aerosols and partly due to

the nonlinear relationship between the ERFaci and AOT under different AOTs. Therefore, this study shows the importance of the impacts of the cloud microphysics module on aerosol distributions through both aerosol wet deposition and AIE.

1 Introduction

35

The aerosol-cloud interaction (ACI) is one of the largest sources of uncertainty in near-term climate projections (Szopa et al., 2021). The radiative forcing related to ACI is estimated from -1.45 Wm^{-2} to -0.25 Wm^{-2}, which is the largest among the various forcing agents (Forster et al., 2021). The major process of the ACI is aerosol nucleation to act as cloud condensation nuclei (CCN) and its subsequent modification of cloud properties through perturbations to cloud droplet number concentration (Twomey, 1977) and to cloud lifetime via water conversion from cloud to precipitation (Albrecht, 1989). On the other hand,

40

in terms of the aerosol itself, wet deposition through rainout and washout often dominates the sink process and determines the spatiotemporal distribution. Because most aerosols are hygroscopic, they are removed from the atmosphere mainly by rainout or in-cloud scavenging (e.g., Henzing et al., 2006). In the rainout process, activated or formed aerosols in individual cloud droplets fall to the ground surface by precipitation. The modeling of rainout strongly affects the spatiotemporal variation and distribution of hygroscopic aerosols such as sulfate, organic aerosols, and sea salt (Textor et al., 2006; Myhre et al., 2013; Gliß

45

et al., 2021). Even for less hydroscopic aerosols such as dust and black carbon (BC), the wet deposition process is important to determine their atmospheric lifetime (Koffi et al., 2016; Sand et al., 2021). Thus, aerosols and clouds are tightly connected to each other, and hence, an elaboration of both the cloud module and aerosol physics module is required to improve ACI in climate models. One of the methods to improve cloud simulations is the use of convection-permitting resolution, which explicitly represent cloud systems with a detailed cloud microphysics scheme (Satoh et al., 2019; Stevens et al., 2019). In very

50

high-resolution models with a horizontal grid size of O (10 km) or less, clouds and precipitation are more realistically represented compared to conventional global models with a grid size of O (100 km) (e.g., Stevens et al., 2019). It is promising that convective cloud systems are better represented with finer model resolution when cumulus parameterizations are avoided (e.g., Vergara-Temprado et al., 2020). However, most global models with convection-permitting resolution do not treat aerosols explicitly or do not deeply evaluate aerosol distributions because of very expensive computational costs (Satoh et al.,

55

2019; Stevens et al., 2019; Coppola et al., 2020).

One of the global models with convection-permitting resolution is Non-hydrostatic Icosahedral Atmospheric Model (NICAM: Tomita and Satoh, 2004; Satoh et al., 2008; Satoh et al., 2014; Kodama et al., 2021) coupled to an aerosol physics module (Suzuki et al., 2008; Dai et al., 2014; Goto, 2014), and the ACI in global cloud resolving simulations has been examined for a

60

decade or more (Suzuki et al., 2008; Sato et al., 2018; Goto et al., 2020). High-resolution simulations of aerosols have various advantages for reproducing the distribution of the observed aerosols (Goto et al., 2015, 2020) and better representing the ACI effect by simulating more realistically the relationship between changes in cloud liquid water path and aerosols (Sato et al., 2018). Especially in the Arctic, the simulated aerosols in the high-resolution model are closer to the observations than those in

the low-resolution model (Ma et al., 2014; Sato et al., 2016; Goto et al., 2020). With further improvements in computing
65   resources, online aerosol calculations in such high-resolution models are highly promising next steps for understanding the
interaction between aerosols, clouds, and precipitation. On the other hand, some issues remain even in global high-resolution
simulations using NICAM (Goto et al., 2020). For example, the difference in the simulated AOT with high- and low-resolution
models is small and estimated to be 3% in a global average, whereas the difference in the simulated aerosol mass concentrations
is large and estimated to be 20% near the source areas. Over remote oceans such as the Southern Ocean, the simulated AOT
70   sometimes exceeds 0.3 in monthly averages, which apparently shows the overestimation of the simulated AOT compared to
the satellite observations. The simulated AOTs include a relatively large bias of 20% compared to the surface-observed results.
Past research indicated that the biases could be partially solved by improving the wet deposition through improved cloud-
precipitation processes.

The main objective of this study is to clarify the impacts of cloud microphysics modules on aerosol distribution. Therefore,
75   this study uses two different types of cloud microphysics schemes in the NICAM. For the evaluation, the simulated aerosols,
clouds, precipitation, and radiation are compared with the observations. In addition, the global budgets for the simulated
aerosols are compared to other models for reference.

Section 2 describes the model and the observations used in this study. Section 3 shows the results of the simulated clouds
(section 3.1), precipitation (section 3.1) and aerosols (sections 3.2 and 3.3) in the numerical experiments using both the NICAM
80   double-moment bulk cloud microphysics module (NDW6) and the NICAM single-moment bulk module with 6 water
categories (NSW6). They are evaluated by a reference obtained from the NICAM with 14 km and 56 km grid spacing in Goto
et al. (2020). Section 4 shows and discusses the impacts of aerosols on radiation through aerosol-radiation interactions (ARIs)
and ACIs by comparing them with references obtained from both models and satellites. Finally, the summary is shown in
section 5.

85   ## 2 Model descriptions and method

2.1 Atmospheric model

The NICAM is a nonhydrostatic atmospheric model (Tomita and Satoh, 2004; Satoh et al., 2008; Satoh et al., 2014) that can
be calculated with a coarse resolution of from 50 km to 200 km (e.g., Dai et al., 2014; Kodama et al., 2021). It is also a global
model with convection-permitting resolution (Satoh et al., 2019) that greatly helps the understanding of atmospheric
90   phenomena related to clouds and precipitation by resolving the interacting behavior of multiple convective systems (Satoh et
al., 2014). The horizontal grid sizes in the NICAM generally range from O(1 km) to O(10 km) and are often set at 14 km for
a useful and effective balance between model complexity and computing resources (Kodama et al., 2014; Kodama et al., 2021;
Seiki et al., 2022). NICAM aerosol simulations with 14 km grid sizes were performed for the entire year (Sato et al., 2018;
Goto et al., 2020). This study improves previous aerosol simulations (Goto et al., 2020) by using an upgraded version of the
95   NICAM (replacing version 16 series with version 19 series, hereafter referred to as NICAM.19) and the sophisticated cloud

microphysics module NDW6 (the original version named NDW6-SK14 was incorporated to NICAM by Seiki and Nakajima, 2014, the updated version named NDW6-S15 were reflected to the version in NICAM.19 by Seiki et al., 2014, 2015, and the current version named NDW6-G23 considers the interaction between the NDW6-S15 and an aerosol module is introduced to NICAM.19 in this study. The details of the NDW6 update are described in Seiki et al., 2022).

100 NICAM.19 is an official version of the NICAM that was released at the end of 2019. After the official release, minor updates in NICAM.19 are continuing. One of the updates of NICAM.19 from NICAM.16 is the vertically high resolution in the standard experiment. The number of vertical layers in NICAM.19 is 78 (15 layers below 2-km height), which is finer than the 38 (10 layers below 2-km height) in NICAM.16. The layer heights at the bottom and top are 33 m and 50 km, respectively, in NICAM.19, whereas they are 81 m and 37 km, respectively, in NICAM.16. The increased vertical levels force the timestep to

105 change from 60 seconds in NICAM.16 to 30 seconds in NICAM.19. Various bugs in NICAM.16 are eliminated in NICAM.19, and the aerosol module in NICAM.19 is also updated (explained in section 2.2).

This study uses the double-moment bulk cloud microphysics scheme NDW6, which is newly coupled to aerosol physics module in this study. For a comparison, the original single-moment bulk cloud microphysics scheme (NSW6: Tomita, 2008; Kodama et al., 2012; Roh and Satoh, 2014) is also used. NSW6 predicts the mass mixing ratios of 6 hydrometeors, i.e., water

110 vapor, cloud water, rain, cloud ice, snow, and graupel. Therefore, the cloud droplet number concentration (CDNC) is assumed to be the same as CCN, which was calculated by coupling with the aerosol physics model using the CCN parameterization proposed by Abdul-Razzak and Ghan (2000). The CDNC is then used for autoconversion and accretion in rain formation. In this way, the ACI for both the stratiform- and convective-cloud systems is incorporated in the cloud microphysics scheme. On the other hand, NDW6 predicts both the mass mixing ratios and the number concentrations of hydrometeors. Prior to this study,

115 NDW6 is not coupled with aerosol physics models and CCN number concentrations at a background level are assumed to be constant globally (Seiki and Nakajima, 2014). In accordance with the nucleation procedure, the background CCN value is replaced with predicted CCN values from the aerosol physics model using the CCN parameterization (Abdul-Razzak and Ghan 2000). In addition, a CDNC value is assumed to be updated to a CCN value only when the CCN value exceeds the CDNC value in a grid box. In this way, NSW6 and NDW6 coupled with the aerosol physics model are affected by the global

120 distribution of aerosols.

Note that autoconversion and accretion, which mainly determine the strength of aerosol lifetime effects (Albrecht, 1989), are different between NSW6 and NDW6. NDW6 uses the parameterization proposed by Seifert and Beheng (2006), and NSW6 uses the parameterization proposed by Khairoutdinov and Kogan (2000), which is updated in this study (cf., Seiki and Roh, 2020). In addition, since NDW6 predicts the CDNC, the CDNC and aerosols are individually transported by advection and

125 removed by reduction terms. In contrast, NSW6 assumes that a change in CCN directly connects with a change in diagnosed CDNC, although rain does not directly change cloud water in this case. Thus, the impact of scavenged aerosols on cloud water is inevitably overestimated in single-moment bulk cloud microphysics schemes. These differences influence the representation of ACI.

Other physical processes in this study are identical to those set in Goto et al. (2020). The advection module is per Miura (2007)
130   and Niwa et al. (2011). The diffusion module is the level-2 Mellor-Yamada-Nakanishi-Niino (MYNN) scheme (Mellor and
Yamada, 1972; Nakanishi and Niino, 2004; Noda et al., 2010). Similar to previous studies using the NICAM (e.g., Satoh et
al., 2010), a cumulus parameterization is not used in this study. The land surface module is the Minimal Advanced Treatments
of Surface Interaction and Runoff (MATSIRO) (Takata et al., 2003). The radiation module is the Model Simulation Radiation
Transfer code (MSTRN-X) (Sekiguchi and Nakajima, 2008). The aerosol module is the Spectral Radiation-Transport Model
135   for Aerosol Species (SPRINTARS) (Takemura et al., 2005; Suzuki et al., 2008), which is explained in section 2.2.
The NICAM-simulated cloud, precipitation, and radiation fluxes at the top of atmosphere (TOA) are evaluated by satellite
products. The satellite-based product of precipitation is provided by version 2.2 of the Global Precipitation Climatology Project
(GPCP) with monthly 2.5°×2.5° grids (Adler et al., 2003). The satellite-based product of the cloud liquid water path (LWP) is
provided by the Multisensor Advanced Climatology (MAC) Total Liquid Water Path L3 with monthly 1°×1° grids (Elsaesser
140   et al., 2017). The ratio of the column precipitation to the sum of the column precipitation and cloud liquid water is calculated
by CloudSat products of cloud liquid water and precipitation liquid water in 2C-RAIN-PROFILE (Lebsock and L'ecuyer,
2011). According to Lebsock and L'ecuyer (2011), this product is more reliable than other Cloudsat products, such as 2C-
RAIN-COLUMN, but this product is retrieved over only the ocean, and CloudSat cannot properly detect signals below a height
of 1 km (Christensen et al., 2013; Huang et al., 2012; Liu, 2002). The cloud optical thickness (COT) is retrieved from the
145   Moderate Resolution Imaging Spectroradiometer (MODIS) for all types of clouds (Platnick et al., 2015). The cloud fraction
(CF) at a low level is estimated from datasets under the International Cloud Climatology Project (ISCCP; Rossow and Schiffer,
1999). The satellite-based radiation fluxes, i.e., outgoing shortwave and longwave radiative flux (hereafter referred to as OSR
and OLR) and shortwave and longwave cloud radiative forcing (hereafter referred to SWCRF and LWCRF), are provided by
the Clouds and the Earth's Radiant Energy System (CERES) experiment onboard Terra and Aqua, as CERES_EBAF_Ed4.1,
150   with 1°×1° grids (Loeb et al., 2009). For the comparisons in this study, these datasets are averaged for the 3 years from 2012-
2014, except for approximately 6 yearly averages (June 2006 to April 2011) in 2C-RAIN-PROFILE.

2.2 Aerosol module

The mass mixing ratios of the major tropospheric aerosols (dust, sea salt, carbonaceous aerosols including organic matter or
OM and BC, and sulfate) and the precursors of sulfate (SO_2 and dimethyl sulfide or DMS) are explicitly calculated in the
155   SPRINTARS-based aerosol module. The details of the aerosol module that is coupled to NICAM are also described elsewhere
(Dai et al., 2014; Goto et al., 2015, 2019, 2020; Goto and Uchida, 2022), but the main three updates in this study are explained
as follows. First, when the CCN number concentration higher than the CDNC is calculated online in the aerosol module, the
value of water supersaturation is positive, and the atmospheric pressure is above 300 hPa, the aerosol nucleation process is
calculated using the CCN number concentration. The vertical fluxes of the simulated hydrometeors, except for water vapor, in
160   the cloud microphysics module are used in the wet deposition for aerosols. Second, the assumption of sulfate in clouds is
modified. In this study, the sulfate formed in the clouds by aqueous-phase oxidation at the current timestep is not scavenged

by the rainout process at the same timestep because the cloud water used in aqueous-phase oxidation is an output at the current timestep. The model timestep is 30 seconds, so this assumption is reasonable in this simulation. This is one of the uncertainties of the modeling, and the assumption has an impact on the simulated sulfate, as shown later. Third, the treatment of dust aerosols

165 is modified according to the latest version of SPRINTARS coupled to MIROC (Takemura et al., 2009; Tatebe et al., 2019). Dust particles in a wide range of sizes (from 0.13 μm to 8.02 μm in mode radii) are divided into bins, and the number of bins is reduced from 10 to 6. In addition, the dependence of the leaf area index (LAI) is a newly introduced function of the dust emissions in the aerosol module. The dust emission is a function of the cube of the wind speed at a height of 10 m, absorbed photosynthesis radiation depending on the LAI, soil moisture, and snow cover by using empirical coefficients that depend on

170 7 regions in the world (Takemura et al., 2009). The empirical coefficients, i.e., threshold values of soil moisture and emission strength, are newly tuned in this study. Except for these updates, the treatment and tuning parameters for the aerosol processes in this study are identical to those in Goto et al. (2020).

The emission fluxes used in this study are the Hemispheric Transport of Air Pollution (HTAP)-v2.2 (Janssen-Maenhout et al., 2015) for BC, organic carbon (OC) and SO_2 from anthropogenic materials and the Global Fire Emission Database (GFED)

175 version 4 (van der Werf et al., 2017) for BC, OC and SO_2 from biomass burning. The ratio of OC to OM is set at 1.6 for anthropogenic activities and 2.6 for biomass burning (Tsigaridis et al., 2014). Secondary organic aerosols (SOAs) are assumed to be particles by multiplying the emission fluxes of isoprene and terpenes provided by the Global Emissions Initiative (GEIA) (Guenther et al., 1990). Parts of SO_2 are emitted from volcanic eruptions (Diehl et al., 2012) and are formed from DMS, which is interactively emitted in the aerosol module (Bates et al., 1987). Sulfate is formed from SO_2 oxidation with a 3-dimensional

180 distribution of monthly oxidants (ozone, H_2O_2 and OH) provided by a chemical transport model (CHASER) coupled to MIROC (Sudo et al., 2002). Emission fluxes for dust (Takemura et al., 2009) and sea salt (Monahan et al., 1986) are interactively calculated in the model using mainly the wind speed at a height of 10 m.

The removal processes, i.e., wet deposition, dry deposition, and gravitational settling, for aerosols are not different from those used in previous studies (Goto et al., 2020; Goto and Uchida, 2022). However, the wet deposition fluxes simulated by the

185 NICAM in this study are directly modulated by the change in the cloud microphysics modules and autoconversion from clouds to precipitation because the wet deposition flux is strongly related to clouds and precipitation outside of the aerosol module (Goto and Uchida, 2022).

For carbonaceous aerosols, SPRINTARS assumes both external and internal mixtures of OM and BC. Pure OM is generated from terpenes as a product of SOA, whereas pure BC is directly emitted from one-half of the amount in anthropogenic sources.

190 SPRINTARS assumes that pure BC is not aged in the atmosphere. The BC and OM components emitted from other emission sources are internally mixed as two types of internal mixtures of OM and BC with BC to OM ratios of 0.3 and 0.15, respectively. BC, OM and sulfate are assumed to have unimodal particle size distributions with mode radii of 0.1 μm for the internal mixture of BC and OM, 0.08 μm for pure OM, 0.054 μm for pure BC and 0.0695 μm for sulfate. For sea salt, there are 4 categories of tracers, with mode radii of 0.178 μm, 0.562 μm, 1.78 μm, and 5.62 μm, that do not age or coagulate with each other in

195 SPRINTARS. The internal mixture of BC and OM, pure OM, sulfate, and sea salt is hydrophilic, whereas the dust and pure BC are hydrophobic. Such physical properties for aerosols in this study are identical to those used in Goto et al. (2020). The optical properties of the aerosols and the calculation methods for ACI in this study are also identical to those used in Goto et al. (2020). The aerosol optical thickness (AOT) at a wavelength of 550 nm is calculated online by the mass concentrations and optical properties for the aerosols and a look-up table prescribed by the Mie theory (Sekiguchi and Nakajima, 2008). To

200 evaluate the radiative forcing of the ARI and ACI, the instantaneous radiative forcing of the ARI (IRFari) and effective radiative forcing for the ACI (ERFaci) are calculated by a general method (e.g., Shindell et al., 2013). The IRFari due to each aerosol species is calculated online by the difference in the radiative fluxes with/without the aerosol species in the radiation module (Goto et al., 2020). The ERFaci due to anthropogenic aerosols only is calculated by the difference in the cloud radiative fluxes between the preindustrial and present conditions of aerosols according to the method proposed by Ghan (2013). The

205 impacts of anthropogenic aerosols on radiative forcing are estimated by the difference between the standard experiment and the extra experiment under preindustrial conditions. In the extra experiment, everything is the same as those in the standard experiment, except that the anthropogenic emission fluxes of BC, OC and SO_2 are set to zero. In all the experiments, the results presented here are the 6-year simulations after the 1-month spinup calculation, which are obtained from the end of the 1-year aerosol online simulations coupled to NSW6. All the experiments in this study are summarized in Table 1.

210 In this study, the simulated aerosols are evaluated by in situ measurements and satellite aerosol products. The climatological observations used in the evaluation of the simulated aerosol mass concentrations are provided by the Interagency Monitoring of Protected Visual Environments (IMPROVE; Malm et al., 1994) program in the United States, the European Monitoring and Evaluation Programme (EMEP) in Europe, the Acid Deposition Monitoring Network in East Asia (EANET) in Asia, and the China Meteorological Administration Atmosphere Watch Network (CAWNET; Zhang et al., 2012) in China. The

215 climatological observations used in the evaluation of the simulated AOT are provided by the Aerosol Robotic Network (AERONET; Holben et al., 1998), SKYNET radiometer network (Nakajima et al., 2020), and China Aerosol Remote Sensing Network (CARSNET; Che et al., 2015). These identical datasets were prepared and used in Goto et al. (2020), which shows the location map and description in Table 1 and Figure 1. In the global aerosol validation, the level 3 AOT product of Collection 6 MODIS onboard the polar-orbiting satellite Terra (MOD08_L3) by Platnick et al. (2015) is used. The AOT is retrieved from

220 the deep blue (Hsu et al., 2013) and dark target (Levy et al., 2013) methods. The uncertainty of the retrieved AOT from both methods is similar to each other (Sayer et al., 2014) and estimated to be ± (0.05 + 0.15*AOT) (Levy et al., 2013). However, satellite-retrieved AOTs are still divergent among different sensors (Petrenko and Ichoku, 2013; Alfaro-Contreras et al., 2017; Wei et al., 2019; Sogacheva et al., 2020), so the level 3 AOT product from collection F15_0031 (V22 level 3) of the Multiangle Imaging Spectroradiometer (MISR) onboard Terra by Kahn et al. (2010) is also used in this study. While MODIS has 36 bands

225 from 0.41 μm to 14 μm, a single view and a broad swath of 2330 km, MISR has four bands (0.45 μm, 0.56 μm, 0.67 μm, and 0.87 μm) with nine cameras with the narrowest swath at 380 km. The uncertainty of MISR-retrieved AOT is estimated to be 0.05 or 0.2*AOT (Kahn et al., 2010). Wei et al. (2019) showed that the MODIS-retrieved AOT is the closest to AERONET, and the MISR-retrieved AOT is the second closest to AERONET among various satellite AOT products. Alfaro-Contreras et

al. (2017) showed that the bias of the AOT between MODIS and MISR is found over the Southern Ocean, where the MISR-

230 retrieved AOT is larger than the MODIS-retrieved AOT due to cloud contamination (Toth et al., 2013). Petrenko and Ichoku (2013) showed the large uncertainty of the MODIS-retrieved AOT over high albedo areas such as desert, snow, and ice surface. In East Asia, the MISR-retrieved AOT is lower than the AERONET-retrieved AOT, but the MODIS-retrieved AOT is higher than the AERONET-retrieved AOT (Kahn et al., 2010). The 3-dimensional distribution of the aerosol extinction coefficients obtained from the Cloud-Aerosol Lidar with Orthogonal Polarization (CALIOP)/Cloud-Aerosol Lidar and Infrared Pathfinder

235 Satellite Observations (CALIPSO) version 3 provided by the NASA Langley Research Center (LaRC) are used in a $1° \times 1°$ grid under clear-sky conditions (Winker et al., 2013). The CALIOP (version 3)-retrieved AOTs are sometimes compared with the MODIS (Collection 6)-retrieved AOTs in previous studies (Kim et al., 2018; Liu et al., 2018; Proestakis et al., 2018). Kim et al. (2018) show that the differences in the CALIOP (version 3)-retrieved AOT and MODIS-retrieved AOT are estimated to be -0.010 over ocean and +0.069 over land due to the inconsistency of the footprint resolution. Compared to the AERONET-

240 retrieved AOT, the CALIOP-retrieved AOT is lower by 0.064. Therefore, over land, the CALIOP-retrieved AOT is underestimated, and the MODIS-retrieved AOT is overestimated. Liu et al. (2018) also showed that the CALIOP-retrieved AOT for polluted days in China is more reliable than the MODIS-retrieved AOT. Therefore, the difference in the retrieved AOT between MODIS, MISR, and CALIOP can be considered as the uncertainty of the satellite retrievals for AOT. These satellite datasets are averaged for the 3 years from 2012-2014.

245 **3 Results and discussion**

3.1 Precipitation and clouds

For simplicity, the simulated products in the numerical experiment with the NDW6 (or NSW6) cloud microphysics module are expressed hereafter as "the NDW6(NSW6)-simulated products". First, the NICAM-simulated (i.e., both NDW6- and NSW6-simulated) precipitation and clouds are evaluated by satellite results. Figure 1 shows the zonal and horizontal

250 distributions of the annual, January and July averages of precipitation. Table 2 includes the global and annual mean values of precipitation, which are estimated to be 3.01 mm day^{-1} (NDW6), 2.78 mm day^{-1} (NSW6), and 2.68 mm day^{-1} (GPCP). These differences among NDW6, NSW6, and GPCP are also found in January and July. The main reason for these differences is the overestimation of NICAM-simulated precipitation over the tropics. This tendency can be found in previous studies using other high-resolution models with finer horizontal resolutions (e.g., Stevens et al., 2019; Wedi et al., 2020).

255 Figure 2 shows the zonal and horizontal distributions of the annual, January and July averages of the LWP over only the oceans. The global and annual mean LWP values over only the oceans (60°S-60°N) are estimated to be 95.8 g m^{-2} (NDW6), 104.4 g m^{-2} (NSW6), and 119.6 g m^{-2} (MAC). The zonal and annual distribution of the NDW6-simulated LWP near the polar regions (> 45°S and > 45°N) is more comparable to the MAC results than to the NSW6 result. This feature is explained by the better reproducibility of supercooled liquid water in low-level mixed-phase clouds (Roh et al., 2020; Seiki and Roh, 2020; Noda et

260 al., 2021). In the other regions, i.e., 45°S-45°N, the NDW6-simulated LWP is not closer to the MAC result compared to the

NSW6 result. However, the seasonal and horizontal biases of the NSW6-simulated LWP are effectively cancelled, and the global and annual mean values of the NSW6-simulated LWP appear closer to the MAC results. In terms of the distribution pattern and seasonal cycle, the NDW6-simulated LWP is closer to the MAC result compared to the NSW6 result. The low bias of the NICAM-simulated LWP over the tropics is caused by underestimation in the western Pacific Ocean.

265 Table 2 includes other cloud information (COT and CF at the low level). Both NDW6- and NSW6-simulated COTs in annual, January and July global mean values are underestimated compared to the MODIS results. This tendency is similar to the results of the LWP. In the spatial distribution, the NDW6-simulated COT has a lower bias over midlatitude to polar regions, whereas the NSW6-simulated COT has a lower bias in other areas (not shown). For CF at the low level, the differences between the NDW6- and NSW6-simulated results are very small, and both results are underestimated compared to the ISCCP results.

270 Therefore, the difference in the cloud microphysics module has almost no impact on the CF.

In summary, the global and annual mean values of the NDW6 simulation include biases of +12% in the precipitation, -20% in the LWP, -45% in the COT, and -28% in the CF at low levels. The biases in the NSW6 simulation have the same sign, but their magnitudes are slightly different (+4% in the precipitation, -13% in the LWP, -35% in the COT, and -27% in the CF at low levels). These mean values are useful for discussing differences among global climate models in terms of the global budget,

275 but they generally include compensation errors in time and space, as explained above. Therefore, the results in NDW6 are generally better and closer to those of the real atmosphere.

3.2 Mass loading of aerosols

NICAM-simulated aerosols are evaluated by statistical metrics, including the Pearson correlation coefficient (PCC), normalized mean bias (NMB), and root-mean-square error (RMSE), defined as (A1), (A2) and (A3) in Appendix A. Figure 3

280 shows scatterplots of the surface mass concentrations of the NICAM-simulated and observed aerosols. For OM, the calculated statistical metrics in NDW6 are 0.847 (PCC), 3.40 µg m^{-3} (RMSE), and -30.4% (NMB), and the difference between NDW6 and NSW6 is very small. For BC, the calculated statistical metrics in NDW6 are 0.904 (PCC), 1.05 µg m^{-3} (RMSE), and -53.4% (NMB). The difference in the simulated BC between NDW6 and NSW6 is also very small. For sulfate, the calculated statistical metrics in NDW6 are 0.807 (PCC), 3.97 µg m^{-3} (RMSE), and -10.4% (NMB), whereas those in NSW6 are 0.853

285 (PCC), 3.67 µg m^{-3} (RMSE), and -3.7% (NMB).

Figure 4 and Table A1 indicate global and annual mean values of column burden, emission, and atmospheric lifetime, which is calculated by the ratio of column burden to total deposition amount. The column burdens of the NDW6- and NSW6-simulated dust range within the uncertainty of the recent models participating in the AeroCom Phase-III project (Gliß et al., 2021). The amount of dust emissions and the dust lifetime in all NICAM simulations range within the uncertainty obtained

290 from the AeroCom models. The difference in the dust column burden between NDW6 and NSW6 is 23%, which is mainly caused by the 10% difference in emissions between NDW6 and NSW6 due to the difference in the simulated wind. Since the dust emission is approximately proportional to the cubic wind speed at a height of 10 m, only a 3.2% difference in the wind speed in the case of a 10 ms^{-1} average causes a 10% difference in the dust emission strength.

For sea salt, the differences in the column burden, emission, and lifetime among the NICAM simulations are not so large and range within the uncertainty of the references. However, the emission flux of the NDW6-simulated sea salt is higher than that of the NSW6-simulated sea salt, whereas the column burden of the NDW6-simulated sea salt is lower than that of the NSW6-simulated sea salt. This is mainly caused by the difference in wet deposition (see Appendix Table A1). The difference in wet deposition is strongly affected by the difference in the ratio of column precipitation to the sum of the column precipitation and column liquid cloud water (RPCW) between NDW6 and NSW6, as shown in Figure 5. The NDW6-simulated RPCW is larger than that of the NSW6 result, which is easy to see from the results of Figures 1 and 2. Because the NSW6-simulated clouds are larger, the NDW6-simulated RPCW is much closer to the CloudSat-retrieved RPCW. An increase in the RPCW leads to an increase in the aerosols that are dissolved into clouds, which fall to the ground as rain drops and are removed from the atmosphere. Therefore, NDW6-simulated clouds and precipitation cause more wet deposition of simulated aerosols compared to the NSW6 results.

Emissions of OM and BC are given from the database, so the differences in the column burden and lifetime are mainly discussed. The column burdens of the NDW6-simulated OM and BC, including WSBC and WIBC, are always lower than the NSW6 results. The lifetimes of the NDW6-simulated OM and BC are always shorter than the NSW6 results. The differences in the column burden as well as the lifetimes of OM and BC between NDW6 and NSW6 are at most 15%. All the results simulated by the NICAM are within the uncertainty of the AeroCom models but are relatively lower than the medians and averages among the AeroCom models. The BC lifetimes are 5.4 days (NDW6) and 6.3 days (NSW6). They range from 2.9 days to 8.7 days (median 5.5 days) in the AeroCom models (Gliß et al., 2021).

Sulfate is a secondary component and is formed from SO_2 oxidation in the atmosphere and within clouds. Its complexity results in different features from other primary species. The column burden of sulfate is 0.45 TgS (NDW6) and 0.52 TgS (NSW6). The results range from 0.22 TgS to 0.98 TgS (0.60 TgS at the median) in the AeroCom models (Gliß et al., 2021). The lifetimes of sulfate are 2.9 days (NDW6) and 3.3 days (NSW6). They range from 1.8 days to 7.0 days (median 4.9 days) in the AeroCom models (Gliß et al., 2021). To understand the difference in the column burden and lifetime of sulfate between different schemes and resolutions, SO_2, as a precursor of sulfate, becomes an important factor. The column burden of NDW6-simulated SO_2 is 0.28 TgS, which is 16% lower than the NSW6 result. Therefore, the difference in the column burden of sulfate between NDW6 and NSW6 is mainly caused by the difference in the column burden of SO_2 because the difference is very small in the wet deposition of sulfate between NDW6 and NSW6 (Table A1). The difference in the column burden of SO_2 between NDW6 and NSW6 is caused by the chemical loss in the aqueous phase (0.7 TgS yr^{-1} or +2%) and gas phase (1.1 TgS yr^{-1} or -7%) and wet deposition (0.4 TgS yr^{-1} or +24%), as shown in Table A1. The differences between NSW6 and HRM are mentioned in Appendix A.

3.3 Aerosol optical products

Figure 6 shows a global comparison of annual, January, and July averages of both NDW6- and NSW6-simulated AOTs with ground-based measurements (AERONET, SKYNET, and CARSNET). The model performance of both NDW6- and NSW6-simulated AOT is very good, with a high correlation (the PCC value is 0.662 to 0.807 in NDW6 and 0.721 to 0.837 in NSW6), moderate uncertainty (the RMSE value is 0.13 to 0.23 in NDW6 and 0.12 to 0.16 in NSW6), and moderate bias (the NMB value is -24.1% to +27.5% in NDW6 and -8.9% to -5.0% in NSW6). These values are much better than those reported in Goto et al. (2020) (e.g., the PCC value of 0.471 to 0.589, the RMSE of 0.21 to 0.23, and the NMB value of -44.1% to -5.4%), as shown in Appendix B.

Figure 7 shows horizontal distributions of the annual averages in AOT in both NICAM simulations under all-sky and clear-sky conditions and satellite observations of MODIS and MISR onboard TERRA. Generally, both NDW6- and NSW6-simulated AOTs are comparable to the satellite results. As shown in Figure 6, the NDW6-simulated AOT is lower than the NSW6 result. The AOT under all-sky conditions tends to be larger than the AOT under clear-sky conditions, mainly because the relative humidity (RH) under all-sky conditions is generally higher than the RH under clear-sky conditions (Dai et al., 2015). Over the outflow regions of North Africa over the Atlantic Ocean, both the NDW6- and NSW6-simulated AOTs are generally comparable to the satellite results. Over East China, Russia, and Central Asia, there are relatively large differences among the NICAM-simulated, MODIS-retrieved and MISR-retrieved AOTs. As explained in section 2.2, over land such as East China, near the Arctic such as Russia, and in desert areas such as Central Asia, the MODIS-retrieved AOTs tend to be higher than the MISR-retrieved AOTs (Kahn et al., 2010; Shi et al., 2011; Petrenko and Ichoko, 2013). Over the Southern Ocean, where the MISR-retrieved AOT includes cloud contamination (Toth et al., 2013; Alfaro-Contreras et al., 2017), both the NDW6-simulated and NSW6-simulated AOTs are lower than the MISR-retrieved results and comparable to the MODIS-retrieved results. The simulated AOT compositions are also compared with the references of the AeroCom models in Appendix C.

Figure 8 indicates the vertical profiles of the aerosol extinction coefficients in regional and annual averages. Since the CALIOP-retrieved results above a 5 km height include some bias (Watson-Parris et al., 2018), the discussion is focused on the results below a 5 km height. Large differences between NDW6 and NSW6 are found in South Asia (India and Southeast Asia), Africa (the coast of North Africa, North Africa, the coast of Central Africa, and South Africa), and South America, where the NDW6-simulated aerosols are lower than the NSW6-simulated results. In South Asia (Figures 8d and 8i), the vertical profiles of both NDW6- and NSW6-simulated aerosol extinction coefficients are comparable to the CALIOP-retrieved results with peak heights of 0.5-1 km. In East China (Figure 8e), the vertical profiles of both NDW6- and NSW6-simulated aerosol extinction coefficients are different from those obtained from CALIOP, which has low aerosols below 2 km height. These CALIOP (version 3) retrieval results may include biases because CALIOP (version 4) improved this underestimation in East China (Kim et al., 2018). Along the coast of North Africa, both NDW6- and NSW6-simulated aerosols are comparable to the CALIOP-retrieved results (Figure 8g), although in the dust source area in North Africa (Figure 8h), they are overestimated

compared to the CALIOP-retrieved results. This may be one problem of CALIOP retrievals over desert areas where the assumed lidar ratio of pure dust is low (Schuster et al., 2012). In the biomass burning areas (the coast of central Africa, South

360   America, and South Africa), as shown in Figures 8(j), 8(k), and 8(l), the heights at which the extinction coefficient decays (called 'decay height') in the CALIOP results are much more reliable than the vertical profiles of the CALIOP-retrieved extinction coefficient because the CALIOP cannot detect the signal below the optically thick layers (Ma et al., 2013). The decay heights of the NICAM-simulated extinction coefficients are lower along the coasts of central Africa and South Africa and higher in South America compared to the CALIOP results. This large bias of the vertical profile indicates a problem of

365   the vertical transport of aerosols originating from biomass burning in the NICAM, which may not be solved by the improvement of the cloud microphysics module and finer resolution of model grids. The differences between NSW6 and HRM are mentioned in Appendix B.

4 Radiative forcing

This section discusses the impacts of aerosols on radiation through ARI and ACI by comparing them with references obtained

370   from both models and satellites. These comparisons verify the usefulness of the NICAM aerosol model coupled to both the NDW6 and NSW6 modules for climate simulations.

4.1 Aerosol-Radiation Interaction (ARI)

Figure 9 shows the shortwave instantaneous radiative forcing of the ARI (IRFari) at the TOA in the NICAM and references. The magnitudes of the IRFari values among all the NICAM-simulated dust values under both all-sky and clear-sky conditions

375   at the TOA are larger than the reference results (Kinne, 2019). For example, the IRFari dust values are calculated to be -0.46 Wm^{-2} (NDW6), -0.57 Wm^{-2} (NSW6), and -0.24 Wm^{-2} (Kinne, 2019). This is partly caused by the weaker absorption of AOT in this study compared to the median value of the AeroCom models, as shown in Figure C1. In contrast, at the surface, the magnitudes of the IRFari values among all the NICAM-simulated dust values under both all-sky and clear-sky conditions are smaller than the results in Kinne (2019). This is inconsistent with the results of the larger column burden and AOT of dust in

380   this study compared to those of the AeroCom models in Figures 4 and C1. The comparison with the results of Kinne (2019) may imply a much higher mass extinction coefficient of the dust or bias of the simulated dust size distribution, as noted by Kok et al. (2017), who concluded that the simulated dust in current global models is too fine. For other absorption components, i.e., POM+WSBC and WIBC, the NSW6-simulated IRFari values are higher than the NDW6 results. Under all-sky conditions, both NDW6- and NSW6-simulated IRFari values due to POM+WSBC and WIBC are positive because of an increase in

385   absorption in the presence of clouds. At the surface, the difference in the IRFari values among all the NICAM simulations has the same tendency as that obtained from the difference in the column burden or AOT. For SOA, as the other component of carbonaceous aerosols and nonlight-absorbing matter, the difference in the IRFari values among all NICAM simulations generally has the same tendency as that obtained from the difference in carbonaceous aerosols. For other nonlight-absorbing components, i.e., sea salt and sulfate, the difference in the IRFari values between all-sky and clear-sky conditions is very small.

390 At the TOA, the magnitudes of the NDW6-simulated IRFari values are lower than those of the NSW6 results. This is consistent with the results of the column burden (Figure 4) and AOT (Figure C1). The IRFari values due to sea salt are estimated to be -0.56 Wm^{-2} (NDW6), -0.65 Wm^{-2} (NSW6), and -0.72 Wm^{-2} (Kinne, 2019). If the estimation by Kinne (2019) is assumed to be real, the NICAM-simulated AOT of sea salt is underestimated by 10-20%, probably because NICAM underestimates the column burden of sea salt, which can be caused by its lower lifetime among the references (Figure 4c). This may suggest that

395 the NICAM-simulated sea salt is more scavenged by wet deposition, possibly due to high precipitation in the NICAM (Figure 1). For sulfate, the IRFari values are estimated to -0.51 Wm^{-2} (NDW6), -0.60 Wm^{-2} (NSW6), and -0.83 Wm^{-2} (Kinne, 2019). This is consistent with the results of lower values of both the column burden and AOT of sulfate among the reference models (Figures 4b and C), which is caused by the lower lifetime of sulfate among the AeroCom models (Figure 4c).

Overall, the IRFari values due to all aerosols under all-sky conditions are estimated to be -1.57 Wm^{-2} (NDW6) and -1.86 Wm^{-2}

400 (NSW6), -1.92 Wm^{-2} (from -3.1 Wm^{-2} to -0.61 Wm^{-2} in Thorsen et al., 2021), and -1.10 Wm^{-2} (Kinne, 2019). The magnitude of the IRFari by Kinne (2019) is lower than the other estimates because the light-absorbing effect is higher in this reference than in the others. The NSW6-simulated IRFari value is close to the reference value obtained from Thorsen et al. (2021) by summarizing both satellite and model results, whereas the NDW6-simulated IRFari value is lower than the median value of the references by approximately 0.4 Wm^{-2}. The difference in the IRFari values between NDW6 and NSW6 is 0.29 Wm^{-2},

405 which is approximately 16% of the total IRFari value in NDW6. For anthropogenic aerosols, the IRFari values under all sky conditions are estimated to be -0.38 Wm^{-2} (NDW6), -0.45 Wm^{-2} (NSW6), and -0.63 Wm^{-2} (from -0.11 Wm^{-2} to -1.00 Wm^{-2} in Thorsen et al., 2021). The difference in IRFari values between NDW6 and NSW6 is 0.07 Wm^{-2}, which is approximately 15% of the total IRFari value in NDW6. The magnitudes of both NDW6- and NSW6-simulated IRFari values range within the uncertainty but are lower than the median of Thorson et al. (2021). This difference in the total IRFari between NDW6 and

410 NSW6 is caused by the difference in the simulated dust, sea salt and sulfate, as shown in section 3. The difference between NICAM and the reference is mainly attributed to the lower value of the column burden of the simulated sulfate. In conclusion, the magnitudes of both the NDW6- and NSW6-simulated IRFari values are within the uncertainty of the references, and the difference in the IRFari values between NDW6 and NSW6 is up to 20%. In addition, the difference in the IRFari values between NDW6 and NSW6 is larger than the difference between the HRM and LRM in Goto et al. (2020), as mentioned in

415 Appendix D. Therefore, the model development of the cloud microphysics module is important.

Figure 10(a) shows the global and annual mean IRFari values due to anthropogenic aerosols. The NICAM-simulated IRFari values (-0.22 Wm^{-2} in NDW6 and -0.26 Wm^{-2} in NSW6) range around the upper limit of the references (-0.25 Wm^{-2}), including both the satellite observations and models in Thorsen et al. (2021), but comparable to the value of -0.25 Wm^{-2} (-0.45 Wm^{-2} to -0.05 Wm^{-2}) shown in IPCC-AR6 (Forster et al., 2021). The difference between NDW6 and NSW6 is calculated to be 0.04

420 Wm^{-2} (approximately 16%). This is because the IRFari values due to anthropogenic aerosols exclude dust, for which there is a relatively large difference between NDW6 and NSW6. Under clear-sky conditions, the NICAM-simulated values (-0.52 Wm^{-2} in NDW6 and -0.60 Wm^{-2} in NSW6) are smaller than the lower limit of the references (-0.67 Wm^{-2}) in Thorsen et al. (2021).

The difference between NDW6 and NSW6 is calculated to be 0.08 Wm^{-2} (approximately 13%). The difference in the anthropogenic IRFari values between NDW6 and NSW6 is up to 15% or 0.08 Wm^{-2}.

425 **4.2 Aerosol-Cloud Interaction (ACI)**

Before evaluating the simulated radiative forcings due to ACI, the simulated cloud radiative forcing (CRF) and total radiation fluxes are compared for model evaluations of radiation budget. As shown in Table 2, the global and January averages of the SWCRF are estimated to be -48.4 Wm^{-2} (NDW6), -49.3 Wm^{-2} (NSW6), and -50.4 Wm^{-2} (CERES), whereas the global and July averages of the SWCRF are estimated to be -41.8 Wm^{-2} (NDW6), -48.7 Wm^{-2} (NSW6), and -44.5 Wm^{-2} (CERES). The

430 difference in the SWCRF between NDW6 and NSW6 is 0.9 Wm^{-2} in January and 6.9 Wm^{-2} in July. The difference in the SWCRF between NICAM and CERES in January is 2.0 Wm^{-2} (NDW6) and 1.1 Wm^{-2} (NSW6), whereas the difference in the SWCRF between NICAM and CERES in July is 2.7 Wm^{-2} (NDW6) and -4.2 Wm^{-2} (NSW6). At 30°S-30°N latitudes and in annual averages, the NDW6-simulated SWCRF values are underestimated compared to the CERES results, whereas the NSW6-simulated SWCRF values are overestimated and more comparable to the CERES results. At other latitudes and in

435 annual averages, the NDW6-simulated SWCRF is comparable to the CERES results, whereas the NSW6-simulated SWCRF values are underestimated compared to the CERES result. The global and annual averages of the SWCRF are estimated to be -42.5 Wm^{-2} (NDW6) -45.9 Wm^{-2} (NSW6), and -45.7 Wm^{-2} (CERES). The NSW6-estimated SWCRF value is highly comparable to the CERES result but includes large compensation errors in the spatiotemporal distribution. The details of the spatiotemporal characteristics are discussed in Appendix E. The NDW6-estimated SWCRF values are concluded to be better

440 than the NSW6 results. For OSR, OLR, and LWCRF, the validation using CERES results is also shown in Appendix E.

Given the verification of the NICAM-simulated SWCRF above, the simulated ACI due to anthropogenic aerosols is discussed by comparing the results between NDW6 and NSW6 under the preindustrial (PI) and the present day (PD) in Figure 10(b). Figure 11 shows the global maps of changes in the simulated AOT, LWP and shortwave ERFaci between PD and PI. Table 3 also shows the average values of those global and selected regions. These show global and annual mean values of effective

445 radiative forcing for aerosol-cloud interactions (ERFaci) due to anthropogenic aerosols. The global annual averages of the ERFaci value are estimated to be -1.34 Wm^{-2} (NDW6) and -0.63 Wm^{-2} (NSW6). Both NDW6- and NSW6-estimated ERFaci values range within the results in IPCC-AR6 (Forster et al., 2021), i.e., -0.84 Wm^{-2} (-1.45 Wm^{-2} to -0.25 Wm^{-2}), but only NDW6-estimated ERFaci values exceeds the results in the Radiative Forcing Model Intercomparison Project (RFMIP) (Smith et al., 2020), i.e., -0.81±0.30 Wm^{-2}. The magnitude of the ERFaci value in NDW6 is larger than that in NSW6 by 0.72 Wm^{-2}

450 (approximately 53% of the ERFaci value in NDW6), whereas the NDW6-simulated aerosol loadings are smaller than the NSW6 results, as shown in the previous sections. The difference in the ERFaci between NDW6 and NSW6 may be partly explained by a nonlinear relationship of the ERFaci to AOT under the different LWPs, as proposed by Carslaw et al. (2013) who argued that even if the aerosol difference between PI and PD is similar, the value of ERFaci can be larger when the aerosol concentration is lower. The NDW6-simulated AOT is lower than the NSW6-simulated results by 20%, as shown in Figure C1.

455 Figure 11 shows that the horizontal distribution of changes in the simulated LWP is generally consistent with changes in the

simulated ERFaci. By increasing the simulated LWP from PI to PD, the negative values of the simulated ERFaci in the industrial regions, such as the United States, Europe, and East Asia, increase. Table 3 shows that the NDW6-estimated ERFaci value is larger negatively than the NSW6-estimated ERFaci by 0.72 Wm^{-2} (Global), 1.23 Wm^{-2} (US), 4.24 Wm^{-2} (Europe), 1.57 Wm^{-2} (East Asia), and 0.87 Wm^{-2} (India). The difference in the simulated susceptibility, defined as a difference in the

460   LWP change against the aerosol change from PD to PI, between NDW6 and NSW6 is key to understand the difference in the ERFaci. Sato et al. (2018) showed that the NICAM coupled to NSW6 at a 14 km grid spacing generally succeeds in reproducing the satellite-retrieved susceptibility on a global scale. The satellite-retrieved susceptibilities are generally negative over ocean and positive over the industrial areas, such as the United States, Europe, and East Asia. In these industrial areas, the NSW6-simulated susceptibilities tend to be negative, whereas the NDW6 results tend to be positive and consistent with satellite results.

465   In India, the difference in the ERFaci between NDW6 and NSW6 is smaller than those in the other industrial areas, probably because both the NDW6- and NSW6-simulated susceptibilities are negative or slightly positive. Notably, the reason for the differences in the susceptibility between NDW6 and NSW6 should be addressed in future studies.

5 Summary

470   To estimate the impacts of cloud microphysics modules on aerosols and their radiative forcing, 6-year simulations of aerosols are performed using two different types of cloud microphysics schemes, i.e., double-moment bulk cloud microphysics module (NDW6) and single-moment bulk module with 6 water categories (NSW6), in NICAM at a 14 km grid spacing. The previous study of Goto et al. (2020) also simulated aerosols at a 14 km grid spacing. The NICAM used in this study was updated from our previous study of Goto et al. (2020), which also simulated aerosols at a 14 km grid spacing in terms of the cloud

475   microphysics module (from NSW6 to NDW6), the vertical resolution (from 38 layers to 78 layers) and some aerosol modules (sulfate and dust).

The model performance of the surface aerosol mass concentrations and AOT are evaluated with in situ measurements by statistical metrics of correlation (PCC), bias (NMB), and uncertainty (RMSE). The model performances of both NDW6-simulated surface mass and NSW6-simulated surface mass as well as AOT are very good, with moderate to high correlation,

480   low to moderate uncertainty, and low to moderate bias. The differences between NDW6 and NSW6 are small, but they are greatly improved from the previous study of Goto et al. (2020). For example, the PCCs between the simulated and observed AOTs in annual averages are 0.807 (NDW6) and 0.837 (NSW6), which are much higher than 0.471 (HRM) and 0.356 (LRM) in Goto et al. (2020). The reason for the performance improvement in this study is not only the update from Goto et al. (2020) but also the increase in available computational resources (using the supercomputer Fugaku in this study), resulting in

485   approximately 12 times faster computation time than the supercomputer K in Goto et al. (2020).

The NDW6-simulated aerosol distributions are generally lower than the NSW6 results. For example, the global and annual mean values of the simulated AOT under all-sky conditions are estimated to be 0.127 (NDW6) and 0.153 (NSW6), which range within the model uncertainty of the AeroCom models. These differences among the NICAM experiments with different

490 cloud microphysics modules, i.e., NDW6 and NSW6, are caused by a different ratio of column precipitation to the sum of the column precipitation and column liquid cloud water or RPCW, which strongly determines the wet deposition in the aerosols. Since the NDW6-simulated LWP is generally lower than the NSW6 result and the NDW6-simulated precipitation is generally comparable to the NSW6 result, the scavenging effect of the aerosols in NDW6 is larger than that in NSW6. The NDW6-simulated RPCW, precipitation and LWP are generally closer to the satellite-retrieved results compared to the NSW6 result, although their global and annual mean values in NDW6 are sometimes no closer to the observation than the NSW6 results due

495 to compensation errors in time and space.

The differences in the dust emissions, dust column burden and SO_2, AOT, and IRFari values for total aerosols between NDW6 and NSW6 are larger. For example, the IRFari values due to all aerosols under all-sky conditions are estimated to be -1.57 Wm^{-2} (NDW6), -1.86 Wm^{-2} (NSW6), and -1.92 Wm^{-2} (from -3.1 Wm^{-2} to -0.61 Wm^{-2} in Thorsen et al., 2021). The difference in IRFari values between NDW6 and NSW6 is 0.29 Wm^{-2}, which is at most 20% of the total IRFari value in NDW6. The large

500 difference is probably caused by the difference in the simulated dust and sulfate in the present study, as shown in section 3. The difference in the dust between NDW6 and NSW6 is mainly caused by the difference in the emission fluxes due to the difference in the simulated wind, whereas those in the sulfate are mainly caused by the wet deposition of SO_2. A large difference among the experiments is also found in the interaction between aerosols and clouds, ERFaci, in which the global annual mean values are estimated to be -1.34 Wm^{-2} (NDW6) and -0.63 Wm^{-2} (NSW6). The difference in the ERFaci values

505 between NDW6 and NSW6 is 0.72 Wm^{-2} (approximately 53% of the ERFaci value in NDW6). This difference is larger than those in the IRFari, which is up to 15% or 0.08 Wm^{-2}. The regional differences in ERFaci between NDW6 and NSW6 are found to be large in the industrial areas, where the NDW6-simulated ERFaci values are negatively larger than the NSW6-simulated results. These differences are mainly caused by the difference in the susceptibility of the LWP to AOT and partly due to a nonlinear relationship between the ERFaci and AOT under different AOTs, as discussed in section 4.

510 In climate simulations, the simulated radiation fluxes, i.e., SWCRF and OSR, are important. Although there are compensation errors in the spatiotemporal distribution, the differences in the global and annual averages between NICAM (NDW6 and NSW6) and CERES are estimated to be at most 3.2 Wm^{-2} (SWCRF and OSR). For longwave radiation, which is not the specific focus of this study, the differences in the global and annual averages between NICAM (NDW6 and NSW6) and CERES are estimated to be at most 6.4 Wm^{-2} (LWCRF) and at most 3.4 Wm^{-2} (OLR). These biases in the radiation fluxes between NICAM

515 and CERES are acceptable for a climate model.

In conclusion, the NICAM at a 14 km grid spacing with both NDW6 and NSW6 cloud microphysics modules for 6 years generally successfully reproduces the observed aerosols. The NDW6-simulated RPCW, precipitation and LWP are generally closer to the satellite-retrieved results compared to the NSW6 result, and thus, the use of NDW6 is recommended in environmental and climate simulations. However, because simulations using NDW6 require 1.5 times more calculation

520 resources, the use of NSW6 is still useful for long-period climate simulations at high resolutions.

Appendix A: Comparisons in the aerosol mass loading between NSW6 in this study and the results in Goto et al. (2020)

As shown in sections 3.2 and 3.3, the evaluation is performed using statistical metrics: the Pearson correlation coefficient (PCC), normalized mean bias (NMB), and root-mean-square error (RMSE). These metrics using the concentration (C) of the observation (*obs*) and the simulation (*sim*) and the sampling number (N) are defined as follows:

$$PCC = \frac{\sum(C_{obs} - \overline{C_{obs}})(C_{sim} - \overline{C_{sim}})}{\sqrt{\sum(C_{obs} - \overline{C_{obs}})^2 \sum(C_{sim} - \overline{C_{sim}})^2}} \quad (A1)$$

$$NMB = \frac{\sum(C_{sim} - C_{obs})}{\sum(C_{obs})} \times 100[\%] \quad (A2)$$

$$RMSE = \sqrt{\frac{\sum(C_{sim} - C_{obs})^2}{N}} \quad (A3)$$

For the mass loading of OM, the statistical metrics obtained in this study are greatly improved compared to the previous study using NICAM.16 (e.g., PCC or 0.847, RMSE of 3.40, and NMB of -29.9 from Goto et al., 2020). For BC, the statistical metrics in this study are not improved from Goto et al. (2020). For sulfate, the values of the PCC and RMSE in this study are close to those in Goto et al. (2020), but the NMB in this study is much lower. Therefore, the model performance for surface aerosol mass concentrations in this study is apparently improved by modifying the sulfur module, as described in section 2.2.

Global and annual mean values of column burden, emission, and atmospheric lifetime are also compared to the results of Goto et al. (2020), as shown in Table A1. The difference in the dust emission and its column burden among different cloud microphysics modules, i.e., between NDW6 and NSW6, is larger than that among different horizontal resolutions, i.e., between the HRM (14 km) and LRM (56 km). The dust lifetime in this study is shorter than that in Goto et al. (2020). The difference is probably caused by the difference in the dust emission scheme, as described in section 2.2. Surely, the global climate model MIROC uses the same dust emission scheme as in this study and has a shorter lifetime among the AeroCom models (Gliß et al., 2021). The decrease in the number of bins from 10 to 6 may reduce the variability of the particle size distribution, move the center of the particle size distribution to coarser sizes, lead to an increase in the amount of deposition, and then reduce the lifetime. For sea salt, the difference in the emission between NSW6 in this study and HRM in Goto et al. (2020) is approximately 11%. This causes the difference in the column burden, although the difference in the lifetime between this study and Goto et al. (2020) is small. For OM and BC, the differences in NSW6 and HRM are small and within the AeroCom models (Gliß et al., 2021).

For sulfate, the column burden is 0.52 TgS (NSW6), 0.38 TgS (HRM) and 0.32 TgS (LRM), which are within the uncertainty among AeroCom models (Gliß et al., 2021). The lifetimes of sulfate are 3.3 days (NSW6), 2.4 days (HRM) and 2.1 days (LRM), which are also within the variability among the AeroCom models (Gliß et al., 2021). The difference in the sulfate column burden between NSW6 and the HRM is larger than the difference among cloud microphysics modules and different horizontal resolutions. This is attributed to a change in the assumption that sulfate forms in clouds by aqueous-phase oxidation, as described in section 2.2. The difference in the column burden of the simulated sulfate among cloud microphysics modules is comparable to that among different horizontal resolutions. For SO₂, the column burden of the simulated SO₂ is 0.33 TgS

(NSW6), 0.33 TgS (HRM), and 0.31 TgS (LRM). Therefore, the difference in the horizontal distribution affects SO$_2$ oxidation and then the column burden of sulfate, whereas the difference in the cloud microphysics module does not affect the chemical

555 budget of SO$_2$ oxidation.

Appendix B: Comparisons in the AOT between NSW6 in this study and the results in Goto et al. (2020)

The scatterplots of the simulated AOT and the surface-observed AOT are shown in Figure 6 in this study and Figure 6 in Goto et al. (2020). The statistical metrics in this study (both NDW6 and NSW6) are much better than those reported in Goto et al. (2020). The PCC value improved from 0.471 (HRM) to 0.837 (NSW6), the RMSE value improved from 0.21 (HRM) to 0.12

560 (NSW6), and the NMB value improved from -20.2% to -5.4%. In the horizontal distribution of the AOT shown in Figure 7, especially over the Southern Ocean, the NSW6-simulated AOT is greatly improved from the results of Figure 5 in Goto et al. (2020). This means that an AOT larger than 0.3 was frequently observed in past NICAM simulations. Over heavy AOT areas, for example, in the Sichuan Basin located in southwest China and the Indo-Gangetic Plain, the NSW6-simulated AOT is generally more comparable to the satellite-retrieved AOTs compared to the results in the HRM in Goto et al. (2020). The

565 improvement in these areas is caused by the increased number of vertical layers below 2 km height from 10 to 15 in this study, as described in section 2.1. The higher vertical resolution causes better performance of the simulated aerosols in the boundary layer by suppressing the artificial dispersion and diffusion of the aerosols near the surface on the basin. This change can be found in not only the AOT but also the column burden and the surface mass concentrations of the aerosols.

At the end of section 3.3, the vertical profiles of the simulated aerosol extinction coefficients are evaluated by CALIOP retrieval

570 results (Figure 8). Due to the increase in the vertical layer from Goto et al. (2020) to the present study, any improvements in the vertical profiles of the simulated aerosols between NSW6 and the HRM are expected to be large, but drastic changes are not found in most regions. Large differences in the vertical profile are found in East China (Figure 8e), the coast of East Asia (Figure 8f), and Southeast Asia (Figure 8i). Along the coast of East Asia, for example, the decay height of the CALIOP-retrieved extinction coefficients is approximately 0.5 km, whereas the decay height of the NSW6-simulated extinction

575 coefficients is approximately 1 km and that of the HRM-simulated extinction coefficients is zero. In this area, the NSW6-simulated results are improved from the HRM-simulated results. In dusty regions such as the coast of northern Africa (Figure 8g) and northern Africa (Figure 9h), the differences in the aerosol profiles between NSW6 and the HRM are small, even though the dust schemes used in NSW6 are different from those in the HRM, as described in section 2.2. Along the coast of central Africa and over South America, both NSW6- and HRM-simulated results still include biases in the vertical profiles. As

580 mentioned in section 3.3, this bias indicates a problem of the vertical transport of aerosols originating from biomass burning in the NICAM, which may not be solved by the finer vertical and horizontal resolutions.

Appendix C: Comparisons of the AOT components between the NICAM and AeroCom models

The simulated AOT compositions are compared with the references of the AeroCom models (Gliß et al., 2021) in Figure C1. All the NICAM-simulated dust AOTs are larger than those obtained from the AeroCom models. Since the column loadings of

Geoscientific
Model Development
Discussions

585 both the NDW6- and NSW6-simulated dust ranges are within the uncertainty among the AeroCom models shown in Figure 4, the dust treatment updates, especially the reduction in the number of bins for dust, may result in a higher mass extinction coefficient of the dust. The uncertainty of the dust AOTs among the AeroCom models is lower than that of other AOTs, probably because the AeroCom models in dusty areas must be tuned by modifying dust emissions to become closer to the satellite results. All the NICAM-simulated sea salt AOTs range within the uncertainty of the AeroCom models, but the mass

590 extinction coefficient of the sea salt tends to be higher than that of the AeroCom models since the column burden of the NICAM-simulated sea salt is lower than that of the AeroCom models. For carbon and sulfate, all the NICAM-simulated AOTs range within the uncertainty of the AeroCom models. For total species, the NICAM-simulated AOTs, except under NDW6 and clear-sky conditions, are larger than the upper range among the AeroCom models. The NDW6-simulated AOTs and the NSW6-simulated AOTs under only clear-sky conditions are close to the median values of the AeroCom models but lower than

595 the averages obtained from the ground-based AERONET measurements and satellites in Figure 3 of Gliß et al. (2021). The NDW6- and NSW6-simulated absorption AOTs also range within the uncertainty of the AeroCom models (Sand et al., 2021) but are lower than the median value of the AeroCom models.

Appendix D: Comparisons in the shortwave IRFari between NSW6 in this study and the results in Goto et al. (2020)

As shown in Figure 9, the NSW6-estimated IRFari values are compared with the HRM-estimated values and references.

600 Generally, the differences in the IRFari values between NSW6 and HRM are similar tendencies to those in the column burden. After the improvement of increased vertical levels and updates aerosol modules, the IRFari values at TOA are changed by +0.27 Wm^{-2} (dust), -0.13 Wm^{-2} (Seasalt), -0.01 Wm^{-2} (WSBC+POM, i.e., BC-containing particles), +0.04 Wm^{-2} (SOA, i.e., pure OM), +0.03 Wm^{-2} (WIBC, i.e., pure BC), -0.14 Wm^{-2} (sulfate), -0.11 Wm^{-2} (only anthropogenic aerosols), and +0.08 Wm^{-2} (all aerosols). At the surface, the IRFari values are changed by +0.45 Wm^{-2} (dust), -0.14 Wm^{-2} (Seasalt), -0.08 Wm^{-2}

605 (BC-containing particles), +0.03 Wm^{-2} (SOA), -0.04 Wm^{-2} (pure BC), -0.12 Wm^{-2} (sulfate), +0.08 Wm^{-2} (only anthropogenic aerosols), and -0.25 Wm^{-2} (all aerosols). The differences in the IRFari magnitude between NSW6 and HRM are generally higher than those among the different cloud microphysics modules (NDW6 and NSW6) and the different horizontal resolutions (HRM and LRM).

For IRFari, due to changes in aerosols from the preindustrial era and the present era, the difference in NSW6 and HRM is

610 +0.03 Wm^{-2} (all-sky) and -0.03 Wm^{-2} (clear-sky), respectively (see Figure 10). Under the all-sky condition, the difference in the anthropogenic IRFari values between NSW6 and HRM is the largest, whereas under the clear-sky condition, the difference in the values between NDW6 and NSW6 is the largest among these differences. This result is mainly caused by the increase in the simulated sulfate in the present study, as shown in Appendix A.

Appendix E: Evaluation of total radiative fluxes in NICAM

615 Figure E1 illustrates the horizontal distribution of the NDW6- and NSW6-simulated and CERES-retrieved SWCRF as annual, January, and July averages. Over the Southern Ocean in January and the North Pacific and Atlantic Oceans in July, the

magnitudes of the SWCRF values are larger than those in other areas and seasons. In these areas, the NDW6-simulated SWCRF values over the Southern Ocean are closer to the CERES results, whereas the NSW6 results are lower than the CERES results. These results are very consistent with the LWP results, as shown in Figure 2. Over southern China, the eastern US, Europe,

620 central Africa, and the coast of Mexico in January and central Africa, the central Pacific Ocean, and central Asia in July, the NDW6-simulated SWCRF values are closer to the CERES results, whereas in Australia in January and in South Asia in July, the NSW6-simulated SWCRF values are closer to the CERES results. Conversely, in these areas, the magnitudes of the NDW6-simulated SWCRF values are underestimated compared to the CERES results, which is caused by the underestimation of the NDW6-simulated clouds. Neither the NDW6- nor the NSW6-simulated SWCRF values are generally comparable to the

625 CERES results in coastal central Africa in January, the outflow in northern Africa in January, the central Pacific Ocean in January, and the Arctic in July. In zonal averages, these biases that are found in various areas may be effectively cancelled. The NDW6-simulated SWCRF values are closer to the CERES-retrieved results, especially for most of the Northern Hemisphere and at 60-90°S latitudes in January and at 30-90°N latitudes and most of the Southern Hemisphere in July. In contrast, the NSW6-simulated SWCRF values are closer to the CERES results, especially at 45°S-10°N latitudes in January

630 and at 0-45°N latitudes in July.

Figure E2 shows the spatiotemporal distribution of the simulated OSR. As shown in Figure E1, the good performance of the NDW6-simulated clouds and SWCRF generally produces closer results to those of CERES in the Southern Ocean, Northern Pacific, and Atlantic Ocean in January. Especially over the ocean, the larger magnitude of the SWCRF yields a larger magnitude of the OSR. Therefore, the biases of the simulated SWCRF directly reflect the results of the simulated OSR. This

635 is also indicated by the comparisons of the zonal distribution of both the SWCRF and OSR. Over land, however, due to limited clouds and large aerosols, radiative impacts due to aerosols can be found. In January, at 30-45°N latitudes, including industrial areas such as eastern China and dusty areas such as central Asia and western China, the NDW6-simulated SWCRF values are comparable to the CERES results, but the NDW6-simulated OSR values are larger than the CERES results. This suggests the overestimation of scattering aerosols, underestimation of light-absorbing aerosols, or overestimation of the surface albedo in

640 the dusty areas. Figure 7 does not suggest overestimation of simulated aerosols compared to the satellite results. Figure C1 shows an underestimation tendency for absorption AOT among the AeroCom models. Therefore, overestimation of the simulated OSR may be caused by the underestimation of simulated light-absorbing aerosols. In July, at 60-90°N latitudes, even though the magnitudes of the NDW6-simulated SWCRF are lower than the CERES results, the NDW6-simulated OSR values are comparable to the CERES results. This may imply the underestimation of the simulated scattering aerosols, which

645 is consistent with the results over the Arctic shown in Figure 12 of Goto et al. (2020), even though the seasonal variation in the simulated aerosols is comparable to the ground-based observations. Other possibilities include the overestimation of light-absorbing aerosols over the Arctic and/or this effect on the decrease in water vapor, but this possibility is inconsistent with the results of Figure C1. Globally, the NDW6-simulated OSR is more comparable to the CERES result than the NSW6 result in terms of annual, January, and July averages, as shown in Table 2. The global and annual averages are calculated to be 98.6

650 Wm^{-2} (NDW6), 102.0 Wm^{-2} (NSW6), and 99.0 Wm^{-2} (CERES).

For longwave radiation, the impacts of ARI are relatively small. Because the NICAM does not explicitly address the interaction between aerosols and ice clouds, the impacts of the ACI on longwave radiation are also small. Here, the results of OLR and LWCRF are briefly discussed using the global averages shown in Table 2. The global and annual averages of LWCRF are calculated to be 21.5 Wm^{-2} (NDW6), 26.8 Wm^{-2} (NSW6), and 27.9 Wm^{-2} (CERES). The NSW6-simulated LWCRF appears

655   closer to the CERES results, especially at 30°S-30°N latitudes. When the horizontal distribution of the LWCRF is examined, compensation errors in terms of longitudes are found. In the western Pacific Ocean, the NSW6-simulated clouds at high levels are remarkably overestimated compared to the CERES results, but in other areas, both the NDW6- and NSW6-simulated LWCRF are underestimated compared to the CERES results. However, because the NDW6-simulated clouds at the high level are not as remarkably overestimated compared to the CERES results, the global average of the NDW6-simulated LWCRF is

660   lower than the CERES results. In the OLR shown in Table 2, the global and annual averages are calculated to be 242.2 Wm^{-2} (NDW6), 236.8 Wm^{-2} (NSW6), and 240.2 Wm^{-2} (CERES). In January and July, the NDW6-simulated OLR appears close to the CERES results, whereas the NSW6-simulated OLR is lower than both the CERES and NDW6 results. As already mentioned, compensation errors in the horizontal distribution arise, but such errors cannot be solved by improvements of the aerosols.

665

Code and data availability

The source codes of NICAM.19 used in this study can be obtained at DOI:10.5281/zenodo.7731449 upon request under general terms and conditions (http://nicam.jp/hiki/?Research+Collaborations). The relevant model results in this study are archived at

670   DOI:10.5281/zenodo.7731486.

Author contributions

DG designed and conducted the numerical experiments and analyses. TS and HY configured the model and prepared the external conditions of the experiments. DG wrote the initial draft of the paper, and all the coauthors (TS, KS, HY, and TT) participated in the discussions of the results and commented on the original manuscript.

675   **Competing interests**

The authors declare that they have no conflicts of interest.

Acknowledgments

References

Abdul-Razzak, H., and Ghan, S. J.: A parameterization of aerosol activation: 2 Multiple aerosol types, J. Geophys. Res., 105, D5, 6837-6844, doi:10.1029/1999JD901161, 2000.

Adler, R. F., Huffman, G. J., Chang, A., Ferraro, R., Xie, P., Janowiak, J., Rudolf, B., Schneider, U., Curtis, S., Bolvin, D., Gruber, A., Susskind, J., and Arkin, P.: The version 2 Global Precipitation Climatology Project (GPCP) monthly

precipitation analysis 1979-present, J. Hydrometeorol., 4, 1147-1167, doi:10.1175/1525-7541(2003)004<1147:TVGPCP>2.0.CO;2, 2003.

Albrecht, B. A.: Aerosols, cloud microphysics, and fractional cloudiness, Science, 245(4923), 1227-1230,
715   http://doi.org/10.1126/science.245.4923.1227, 1989.

Alfaro-Contreras, R., Zhang, J., Reid, J. S., and Chistopher, S.: A study of 15-year aerosol optical thickness and direct shortwave aerosol radiative effect trends using MODIS, MISR, CALIOP and CERES. Atmos. Chem. Phys., 17, 13849-13868, https://doi.org/10.5194/acp-17-13849-2017, 2017.

Bates, T. S., Charlson, R. J., and Gammon, R. H.: Evidence for the climate role of marine biogenic sulphur, Nature, 329, 319–
720   321, 1987.

Berry, E. X.: Cloud droplet growth by collection, J. Atmos. Sci., 24, 688-701, 1967.

Carslaw, K. S., Lee, L. A., Reddington, C. L., Pringle, K. L., Rap, A., Forster, P. M., Mann, G. W., Spracklen, D. V., Woodhouse, M. T., Regayre, L. A., and Pierce, J. R.: Large contribution of natural aerosols to uncertainty in indirect forcing, Nature, 503, 67-71, doi:10.1038/nature12674, 2013.

725   Che, H., Zhang, X.-Y., Xia, X., Goloub, P., Holben, B., Zhao, H., Wang, Y., Zhang, X.-C., Wang, H., Blarel, L., Damiri, B., Zhang, R., Deng, X., Ma, Y., Wang, T., Geng, F., Qi, B., Zhu, J., Yu, J., Chen, Q., and Shi, G.: Ground-based aerosol climatology of China: aerosol optical depths from the China Aerosol Remote Sensing Network (CARSNET) 2002–2013, Atmos. Chem. Phys., 15, 7619–7652, doi:10.5194/acp-15-7619-2015, 2015.

Christensen, M. W., Stephens, G. L., and Lebsock, M. D.: Exposing biases in retrieved low cloud properties from CloudSat:
730   A guide for evaluating observations and climate data, J. Geophys. Res. Atmos., 116, 12120-12131, doi:10.1002/2013JD020224, 2013.

Chung, S. H., and Seinfeld, J. H.: Global distribution and climate forcing of carbonaceous aerosols, J. Geophys. Res., 107(D19), 4407, doi:10.1029/2001JD001397, 2002.

Coppola, E., Sobolowski, S., Pichelli, E., Raffaele, F., Ahrens, B., Ander, I., Ban, N., Bastin, S., Belda, M., Belusic, D., Caldas-
735   Alvarez, A., Cardoso, R. M., Davolo, S., Dobler, A., Fernandez, J., Fita, L., Fumiere, Q., Giorgi, F., Goergen, K., Güttler I., Halenka, T., Heinzeller, D., Hodnebrog, Ø., Jacob, D., Kartsios, S., Katragkou, E., Kendon, E., Khodayar, S., Kunstmann, H., Knist, S., Lavín-Gullón, A., Lind, P., Lorenz, T., Maraun, D., Marelle, L., van Meijgaard, E., Milovac, J., Myhre, G., Panitz, H.-J., Piazza, M., Raffa, M., Raub, T., Rockel, B., Schär, C., Sieck, K., Soares, P. M. M., Somot, S., Srnec, L., Stocchi, P., Tölle, M. H., Truhetz, H., Vautard, R., de Vries, H., and Warrach-Sagi, K.: A first-of-its-kind
740   multi-model convection permitting ensemble for investigating convective phenomena over Europe and the Mediterranean, Clim. Dyn., 55, 3-34, https://doi.org/10.1007/s00382-018-4521-8, 2020.

Dai, T., Goto, D., Schutgens, N. A. J., Dong, X., Shi, G., and Nakajima, T.: Simulated aerosol key optical properties over global scale using an aerosol transport model coupled with a new type of dynamic core. Atmos. Environ., 82, 71-82, https://doi.org/10.1016/j.atmosenv.2013.10.018, 2014.

745   Dai, T., Shi, G., and Nakajima, T.: Analysis and evaluation of the global aerosol optical properties simulated by an online aerosol-coupled non-hydrostatic icosahedral atmospheric model, Adv. Atmos. Sci., 32(6), 743–758, doi: 10.1007/s00376-014-4098-z, 2015.

Diehl, T., Heil, A., Chin, M., Pan, X., Streets, D., Schulz, M., and Kinne, S.: Anthropogenic, biomass burning, and volcano emissions of black carbon, organic carbon, and SO_2 from 1980 to 2010 for hindcast model experiments, Atmos. Chem.
750   Phys. Discuss., 12, 24895-24954, doi:10.5194/acpd-12-24895-2012, 2012.

Elsaesser, G. S., O'Dell, C. W., Lebsock, M. D., Bennartz, R., Greenwald, T. J., and Wentz, F. J.: The multisensor advanced climatology of liquid water path (MAC-LWP). J. Clim., 30(24), 10193–10210. https://doi.org/10.1175/JCLI-D-16-0902.1, 2017.

Forster, P., Storelvmo, T., Armour, K., Collins, W., Dufresne, J.-L., Frame, D., Lunt, D.J., Mauritsen, T., Palmer, M. D.,
755   Watanabe, M., Wild, M., and Zhang, H.: The Earth's Energy Budget, Climate Feedbacks, and Climate Sensitivity. In Climate Change 2021: The Physical Science Basis. Contribution of Working Group I to the Sixth Assessment Report of the Intergovernmental Panel on Climate Change [Masson-Delmotte, V., Zhai, P., Pirani, A., Connors, S.L., Péan, C., Berger, S., Caud, N., Chen, Y., Goldfarb, L., Gomis, M. I., Huang, M., Leitzell, K., Lonnoy, E., Matthews, J. B. R., Maycock, T. K., Waterfield, T., Yelekçi, O., Yu, R., and Zhou, B. (eds.)]. Cambridge University Press, Cambridge,
760   United Kingdom and New York, NY, USA, pp. 923–1054, doi:10.1017/9781009157896.009, 2021.

Hsu, N. C., Jeong, M. J., Bettenhausen, C., Sayer, A. M., Hansell, R., Seftor, C. S., Huang, J., and Tsay, S. C.: Enhanced Deep Blue aerosol retrieval algorithm: the second generation. J. Geophys. Res.-Atmos. 118, 9296–9315, 2013.

Ghan, S. J.: Technical Note: Estimating aerosol effects on cloud radiative forcing, Atmos. Chem. Phys., 13, 9971-9974, doi:10.5194/acp-13-9971-2013, 2013.

765   Gliß J., Mortier, A., Schulz , M., Andrews, E., Balkanski, Y., Bauer, S. E., Benedictow, A. M. K., Bian, H., Checa-Garcia, R., Chin, M., Ginoux, P., Griesfeller, J. J., Heckel, A., Kipling, Z., Kirkevåg, A., Kokkola, H., Laj, P., Le Sager, P., Lund, M. T., Myhre, C. L., Matsui, H., Myhre, G., Neubauer, D., van Noije, T., North, P., Olivié, D. J. L., Rémy, S., Sogacheva, L., Takemura, T., Tsigaridis, K., and Tsyro, S. G.: AeroCom phase III multi-model evaluation of the aerosol life cycle and optical properties using ground- and space-based remote sensing as well as surface in situ observations. Atmos. Chem.
770   Phys., 21, 87-128, https://doi.org/10.5194/acp-21-87-2021, 2021.

Goto, D.: Modeling of black carbon in Asia using a global-to-regional seamless aerosol-transport model, Environ. Pol., 195, 330-335, http://dx.doi.org/10.1016/j.envpol.2014.06.006, 2014.

Goto, D., Nakajima, T., Takemura, T., and Sudo, K.: A study of uncertainties in the sulfate distribution and its radiative forcing associated with sulfur chemistry in a global aerosol model, Atmos. Chem. Phys., 11, 10889-10910, doi:10.5194/acp-11-
775   10889-2011, 2011.

Goto, D., Oshima, N., Nakajima, T., Takemura, T., and Ohara, T.: Impact of the aging process of black carbon aerosols on their spatial distribution, hygroscopicity, and radiative forcing in a global climate model, Atmos. Chem. Phys. Discuss., 12, 29801-29849, doi:10.5194/acpd-12-29801-2012, 2012.

24

Geoscientific
Model Development
Discussions

Goto, D., Dai, T., Satoh, M., Tomita, H., Uchida, J., Misawa, S., Inoue, T., Tsuruta, H., Ueda, K., Ng, C.F.S., Takami, A.,
780   Sugimoto, N., Shimizu, A., Ohara, T., and Nakajima,T.: Application of a global nonhydrostatic model with a stretched-
       grid system to regional aerosol simulations around Japan, Geosci. Model Dev., 8, 235-259. Doi:10.5194/gmd-8-235-
       2015, 2015.

Goto, D., Kikuchi, M., Suzuki, K., Hayasaki, M., Yoshida, M., Nagao, T. M., Choi, M., Kim, J., Sugimoto, N., Shimizu, A.,
       Oikawa, E., and Nakajima, T.: Aerosol model evaluation using two geostationary satellites over East Asia in May 2016,
785   Atmos. Res., 217, 93-113, doi:10.1016/j.atmosres.2018.10.016, 2019.

Goto, D., Sato, Y., Yashiro, H., Suzuki, K., Oikawa, E., Kudo, R., Nagao, T. M., and Nakajima, T.: Global aerosol simulations
       using NICAM.16 on a 14 km grid spacing for a climate study: improved and remaining issues relative to a lower-
       resolution model. Geosci. Model Dev., 13, 3731-3768, doi:10.5194/gmd-13-3731-2020, 2020.

Goto, D., and Uchida, J.: Uncertainty in Aerosol Rainout Processes Through the Case of the Radioactive Materials Emitted by
790   the Fukushima Dai-ichi Nuclear Power Plant in March 2011. J. Meteorol. Soc. Japan., 100(1), 197-
       217, doi:10.2151/jmsj.2022-010, 2022.

Guenther, A., Hewitt, C. N., Erickson, D., Fall, R., Geron, C., Graedel, T., Harley, P., Klinger, L., Lerdau, M., McKay, W. A.,
       Pierce, T., Scholes, B., Steincrecher, R., Tallamraju, R., Taylor, J., and Zimmerman, P. A.: Global-Model of Natural
       Volatile Organic-Compound Emissions, J. Geophys. Res., 100, 8873–8892, 1995.

795 Henzing, J. S., Olivié, D. J. L., and van Velthoven, P. F. J.: A parameterization of size resolved below cloud scavenging of
       aerosols by rain, Atmos. Chem. Phys., 6, 3363-3375, https://doi.org/10.5194/acp-6-3363-2006, 2006.

Holben, B. N., Eck, T. F., Slutsker, I., Tanré, D., Buis, J. P., Setzer, A., Vermote, E., Reagan, J. A., Kaufman, Y., Nakajima,
       T., Lavenu, F., Jankowiak, I., and Smirnov, A.: AERONET – A federated instrument network and data archive for aerosol
       characterization, Rem. Sens. Environ., 66, 1-16, 1998.

800 Huang, Y., Siems, S. T., Manton, M. J., Hande, L. B., and Haynes, J. M.: The structure of low-altitude clouds over the Southern
       Ocean as seen by CloudSat, J. Clim., 25, 2535-2546, doi:10.1175/JCLI-D-11-00131.1, 2012.

Huneeus, N., Schulz, M., Balkanski, Y., Griesfeller, J., Prospero, J., Kinne, S., Bauer, S., Boucher, O., Chin, M., Dentener, F.,
       Diehl, T., Easter, R., Fillmore, D., Ghan, S., Ginoux, P., Grini, A., Horowitz, L., Koch, D., Krol, M. C., Landing, W.,
       Liu, X., Mahowald, N., Miller, R., Morcrette, J.-J., Myhre, G., Penner, J., Perlwitz, J., Stier, P., Takemura, T., and Zender,
805   C. S.: Global dust model intercomparison in AeroCom phase I, Atmos. Chem. Phys., 11, 7781-7816, doi:10.5194/acp-
       11/7781-2011, 2011.

Janssens-Maenhout, G., Crippa, M., Guizzardi, D., Dentener, F., Muntean, M., Pouliot, G., Keating, T., Zhang, Q., Kurokawa,
       J., Wankmüller, R., Denier van der Gon, H., Kuenen, J. J. P., Klimont, Z., Frost, G., Darras, S., Koffi, B., and Li, M.:
       HTAP_v2.2: a mosaic of regional and global emission grid maps for 2008 and 2010 to study hemispheric transport of air
810   pollution, Atmos. Chem. Phys., 15, 11411–11432, 2015.

25

Kahn, R. A., Gaitley, B. J., Garay, M. J., Diner, D. J., Eck, T. F., Smirnov, A., and Holben, B. N.: Multiangle Imaging SpectroRatiometer global aerosol product assessment by comparison with the Aerosol Robotic Network, J. Geophys. Res., 115, D23209, doi:10.1029/2010JD014601, 2010.

Khairoutdinov, M., and Kogan, Y.: A new cloud physics parameterization in a large-eddy simulation model of marine stratocumulus. Mon. Wea. Rev., 128, 229–243, 2000.

Kim, M. -H., Kin, S. -W., Yoon S. -C., and Omar, A. H.: Comparison of aerosol optical depth between CALIOP and MODIS-Aqua for CALIOP aerosol subtypes over the ocean, J. Geophys. Res. Atmos., 118, 13241-13252, doi:10.1002/2013JD019527, 2013.

Kim, M. -H., Omar, A. H., Tackett, J. L., Vaughan, M. A., Winker, D. M., Trepte, C. R., Hu Y., Liu, Z., Poole, L. R., Pitts, M. C., Kar, J., and Magill, B. E.: The CALIPSO version 4 automated aerosol classification and lidar ratio selection algorithm, Atmos. Meas. Tech., 11, 6107-6135, https://doi..org/10.5194/amt-11-6107-2018, 2018.

Kinne, S.: Aerosol radiative effects with MACv2, Atmos. Chem. Phys., 19, 10919-10959, doi:10.5194/acp-19-10919-2019, 2019.

Kodama C., Noda, A. T., and Satoh, M.: An Assessment of the cloud signals simulated by NICAM using ISCCP, CALIPSO, and CloudSat satellite simulators, J. Geophys. Res, doi:10.1029/2011JD017317, 2012.

Kodama, C., Yamada, Y., Noda, A. T., Kajikawa, Y., Nasuno, T., Yamaura, T., Takahashi, H. G., Hara, M., Kawatani, Y., Satoh, M., and Sugi, M.: A 20-year climatology of a NICAM AMIP-type simulation. J. Meteorol. Soc. Japan. Ser. II 93, 393-424, doi:10.2151/jmsj.2015-024, 2015.

Kodama, C., Ohno, T., Seiki, T., Yashiro, H., Noda, A. T., Nakano, M., Yamada, Y., Roh, W., Satoh, M., Nitta, T., Goto, D., Miura, H., Nasuno, T., Miyakawa, T., Chen, Y.-W., and Sugi, M.: The non-hydrostatic global atmospheric model for CMIP6 HighResMIP simulations (NICAM16-S): Experimental design, model description, and sensitivity experiments. Geosci. Model Dev.,14, 795-820, doi:10.5194/gmd-14-795-2021, 2021.

Koffi, B., Schulz, M., Bréon, F. -M., Dentener, F., Steensen, B. M., Griesfeller, J., Winker, D., Balkanski, Y., Bauer, S. E., Chin, M., Diehl, T., Easter, R., Ghan, S., Hauglustaine, D. A., Iversen T., Kirkevåg, A., Liu, X., Lohmann, U., Myhre, G., Rasch, P., Seland, Ø., Skeie, R. B., Steenrod, S. D., Stier, P., Tackett, J., Takemura, T., Tsigaridis, K., Vuolo, M. R., Yoon, J., and Zhang, K.: Evaluation of the aerosol vertical distribution in global aerosol models through comparison against CALIOP measurements: AeroCom phase II results, J. Geophys. Res. Atmos., 121, 7254-7283, doi:10.1002.2015JD024639, 2016.

Lebsock M. D., and L'Ecuyer, T. S.: The retrieval of warm rain from CloudSat, J. Geophys. Res. Atmos., 116, D20, https://doi.org/10.1029/2011JD016076, 2011.

Levy, R. C., Mattoo, S., Munchak, L. A., Remer, L. A., Sayer, A. M., Patadia, F., and Hsu, N. C.: The Collection 6 MODIS aerosol products over land and ocean. Atmos. Meas. Tech. 6, 2989–3034, https://doi.org/10.5194/amt-6-2989-2013, 2013.

Liu, B., Ma Y., Gong, W., Zhang, M., Wang, W., and Shi, Y.: Comparison of AOD from CALIPSO, MODIS, and Sun Photometer under different conditions over Central China, Sci. Rep., 8:10066, doi:10.1038/s41598-018-28417-7, 2018.

26

845 Liu, Y.: Impacts of active satellite sensors' low-level cloud detection limitations on cloud radiative forcing in the Arctic, Atmos.
      Chem. Phys., 22, 8181-8173, https://doi/org/10.5194/acp-22-8151-2022, 2022.

Loeb, N. G., Wielicki, B. A., Doelling, D. R., Smith, D. R., Keyes, D. F., Kato, S., Manalo-Smith, N., and Wong, T.: Toward
      optimal closure of the Earth's top-of-atmosphere radiation budget. J. Clim., 22, 748-766, doi:10.1175/2008JCLI2637.1.,
      2009.

850 Ma, X., Bartlett, K., Harmon, K., and Yu, F.: Comparison of AOD between CALIPSO and MODIS: significant differences
      over major dust and biomass burning regions, Atmos. Meas. Tech., 6, 2391-2401, doi:10.5194/amt-6-2391-2013, 2013.

Ma, P.-L., Rasch, P. J., Fast, J. D., Easter, R. C., Gustafson Jr., W. I., Liu, X., Ghan S. J., and Singh, S.: Assessing the CAM5
      physics suite in the WRF-Chem model: implementation, resolution sensitivity, and a first evaluation for regional case study,
      Geosci. Model Dev., 7, 755-778, doi:10.5194/gmd-7-755-2014, 2014.

855 Ma, P. -L., Rasch, P. J., Chepfer, H., Winker, D. M., and Ghan, S. J.: Observational constraint on cloud susceptibility weakened
      by aerosol retrieval limitations, Nat. Comm., 9, 2640, doi:10.1038/s41467-018-05028-4, 2018.

Malm, W. C., Sislerm J. F., Huffmann, D., Eldred, R. A., and Cahill, T. A.: Spatial and seasonal trends in particle concentration
      and optical extinction in the United States, J. Geophys. Res., 99, 1347-1370, https://doi.org/10.1029/93JD02916. 1994.

Mellor, G. L., and Yamada, T.: A hierarchy of turbulence closure models for planetary boundary layers, J. Atmos. Sci., 31,
860   1791–1806, doi: 10.1175/1520-0469(1974)031<1791:AHOTCM>2.0.CO;2, 1974.

Miura, H.: An upwind-biases conservative advection scheme for spherical hexagonal-pentagonal grids, Mon. Wea. Rev., 135,
      4038-4044, 2007.

Morrison, H., Thompson, G., and Tatarskii, V.: Impact of cloud microphysics on the development of trailing stratiform
      precipitation in a simulated squall line: comparison of one- and two-moment schemes, Mon. Wea. Rev., 137, 991-1007,
865   doi:10.1175/2008MWR2556.1, 2008.

Myhre G., Samset, B. H., Schulz, M., Balkanski, Y., Bauer, S., Berntsen, T. K., Bian, H., Bellouin, N., Chin, M., Diehl, T.,
      Easter, R. C., Feichter, J., Ghan, S. J., Hauglustaine, D., Iversen, T., Kinne, S., Kirkevåg, A., Lamarque, J. -F., Lin, G.,
      Liu, X., Lund, M.T., Luo, G., Ma, X., van Noije, T., Penner, J.E., Rasch, P. J., Ruiz, A., Seland, Ø., Skeie, R. B., Stier,
      P., Takemura, T., Tsigaridis, K., Wang, P., Wang, Z., Xu, L., Yu, H., Yu, F., Yoon, J.-H., Zhang, K., Zhang, H., and
870   Zhou, C.: Radiative forcing of the direct aerosol effect from AeroCom Phase II simulations, Atmos. Chem. Phys. 13,
      1853-1877, doi:10.5184/acp-13-1853-2013, 2013.

Monahan, E. C., Spiel, D. E., and Davidson, K. L.: A model of marine aerosol generation via whitecaps and wave disruption,
      in Oceanic Whitecaps and Their Role in Air-Sea Exchange Processes, edited by E. C. Monahan and G. M. Niocaill, pp.
      167-174, Springer, New York, 1986.

875 Nakajima, T., Campanelli, M., Che, H., Estellés, V., Irie, H., Kim, S.-W., Kim, J., Liu, D., Nishizawa, T., Pandithurai, G.,
      Vijay Kumar Soni, V. K., Thana, B., Tugjsurn, N. -T., Aoki, K., Sujung Go, S., Hashimoto, M., Higurashi, A., Kazadzis,
      S., Khatri P., Kouremeti, N., Kudo, R., Marenco, F., Momoi, M., Ningombam, S. S., Ryder, C. L., Uchiyama, A., and

Yamazaki, A.: An overview of and issues with sky radiometer technology and SKYNET, Atmos. Meas. Tech., 13, 4195-4218, doi:10.5194/amt-13-4195-2020, 2020

880 Nakanishi, M., and Niino, H.: An improved Mellor–Yamada level 3 model with condensation physics: its design and verification, Bound. Layer Meteor., 112, 1–31, doi:10.1023/B:BOUN.0000020164.04146.98, 2004.

Niwa, Y., Tomita, H., Satoh, M., and Imasu, R.: A three-dimensional icosahedral grid advection scheme preserving monotonicity and consistency with continuity for atmospheric tracer transport, J. Meteor. Soc. Jpn., 89, 255–268, doi: 10.2151/jmsj.2011-306, 2011.

885 Noda, A. T., Oouchi, K., Satoh, M., Tomita, H., Iga, S., and Tsushima, Y.: Importance of the subgrid-scale turbulent moist process: Cloud distribution in global cloud-resolving simulations, Atmos. Res., 96, 208–217, doi:10.1016/j.atmosres.2009.05.007, 2010.

Noda, A., Seiki, T., Roh, W., Satoh, T., and Ohno, T.: Improved representation of low-level mixed-phase clouds in a global cloud-system-resolving simulation, J. Geophys. Res. Atmos, 126, e2021JD035223,
890 https://doi.org/10.1029/2021JD035223, 2021.

Petrenko, M., and Ichoku, C.: Coherent uncertainty analysis of aerosol measurements from multiple satellite sensors, Atmos. Chem. Phys., 13, 6777-6805, doi:10.5194/acp-13-6777-2013, 2013.

Platnick, S., Hubanks, P., Meyer, K., and King, M. D.: MODIS Atmosphere L3 Monthly Product. NASA MODIS Adaptive Processing System, Goddard Space Flight Center, USA: http://dx.doi.org/10.5067/MODIS/MOD08_M3.006, 2015.

895 Roh, W., and Satoh, M.: Evaluation of precipitating hydrometeor parameterizations in a single-moment bulk microphysics scheme for deep convective systems over the Tropical Central Pacific, J. Atmos. Sci., 77, 3781-3801, https://doi.org/10.1175/JAS-D-13-0252.1, 2014.

Roh, W., Satoh, M., Hashino, T., Okamoto, H., and Seiki, T.: Evaluations of the thermodynamic phases of clouds in a cloud-system-resolving model using CALIPSO and a satellite simulator over the Southern Ocean, J. Atmos. Sci., 77, 3781-
900 3801, https://doi.org/10.1175/JAS-D-19-0273.1, 2020.

Rossow, W. B., and Schiffer, R. A.: Advances in understanding clouds from ISCCP. Bulletin of the American Meteorological Society, 80, 2261–2287. https://doi.org/10.1175/1520-0477(1999)080<2261:AIUCFI>2.0.CO;2, 1999.

Proestakis, E., Amiridis, V., Marinou, E., Georgoulias, A. K., Solomos, S., Kazadzis, S., Chimot, J., Che, H., Alexandri, G., Binietoglou,I., Daskalopoulou, V., Kourtidis, K. A., de Leeuw, G., and van der A, R. J.: Nine-year spatial and temporal
905 evolution of desert dust aerosols over South and East Asia as retrieved by CALIOP, Atmos. Chem. Phys., 18, 1337-1362, https://doi.org//10.5194/acp-18-1337-2018, 2018.

Sand, M., Samset, B. H., Myhre, G., Gliß, J., Bauer, S. E., Bian, H., Chin, M., Checa-Garcia, R., Ginoux, P., Kipling, Z., Kirkevåg, A., Kokkola, H., Sager, P. L., Lund, M. T., Matsui, H., van Noije, T., Olivié, D. J. L., Remy, S., Schulz, M., Stier, P., Stjern, C. W., Takemura, T., Tsigaridis, K., Tsyro, S. G., and Watson-Parris, D.: Aerosol absorption in global
910 models from AeroCom Phase III. Atmos. Chem. Phys., 21, 15929–15947, doi:10.5194/acp-21-15929-2021, 2021.

Sato, Y., Goto, D., Michibata, T., Suzuki, K., Takemura, T., Tomita, H., and Nakajima, T.: Aerosol effects on cloud water amounts were successfully simulated by a global cloud-system resolving model, Nature Com., 9: 985, doi:10.1038/s41467-018-03379-6, 2018.

Satoh, M., Matsuno, T., Tomita, H., Miura, H., Nasuno, T., and Iga, S.: Nonhydrostatic icosahedral atmospheric model (NICAM) for global cloud resolving simulations. J. Comput. Phys., 227, 3486-3514. Doi:10.1016/j.jcp.2007.02.006, 2008.

Satoh, M., Inoue, T., and Miura, H.: Evaluations of cloud properties of global and local cloud system resolving models using CALIPSO and CloudSat simulators, J. Geophys. Res., 115, D00H14, https://doi.org/10.1029/2009JD012247, 2010.

Satoh, M., Tomita, H., Yashiro, H., Miura, H., Kodama, C., Seiki, T., Noda, A.T., Yamada, Y., Goto, D., Sawada, M., Miyoshi, T., Niwa, Y., Hara, M., Ohno, T., Iga, S., Arakawa, T., Inoue, T., and Kubokawa, H.: The non-hydrostatic icosahedral atmospheric model: description and development. Prog. Earth. Plan. Sci., 1, 18-49. Doi:10.1186/s40645-014-0018-1, 2014.

Satoh, M., Stevens, B., Judt, F., and Khairoutdinov, M., Lin, S. -J., Putman, W. M., and Düben, P.: Global Cloud-Resolving Models, Curr. Clim. Change Rep., 5, 172-184, doi:10.1007/s40461-019-00131-0, 2019.

Sayer, A. M., Munchak, L. A., Hsu, N. C., Levy, R. C., Bettenhausen, C., and Jeong, M.-J.: MODIS collection 6 aerosol products: comparison between aqua's e-deep blue, dark target, and "merged" data sets, and usage recommendations. J. Geophys. Res.-Atmos. 119, 13965–13989, 2014.

Schuster, G. L., Vaughan, M., MacDonnell, D., Su, W., Winker, D., Dubovik, O., Lapyonok, T., and Trepte, C.: Comparison of CALIPSO aerosol optical depth retrievals to AERONET measurements, and a climatology for the lidar ratio of dust, Atmos. Chem. Phys., 12, 7431-7452, doi:10.5194/acp-12-7431-2012, 2012.

Seifert, A., and Beheng, K. D.: A two-moment cloud microphysics parameterization for mixed-phase clouds. Part 1: Model description. Meteorol. Atmos. Phys., 92(1), 45–66. https://doi.org/10.1007/s00703-005-0112-4, 2006.

Seiki, T., and Nakajima, T.: Aerosol effects of the condensation process on a convective cloud simulation. Journal of the Atmospheric Sciences, 71 (2), 833–853. https://doi.org/10.1175/JAS-D-12-0195.1, 2014.

Seiki, T., Kodama, C., and Noda, A. T.: Improvement in global cloud-system-resolving simulations by using a double-moment bulk cloud microphysics scheme, J. Clim., 28, 2405-2419, doi:10.1175/JCLI-D-14-00241.1, 2015.

Seiki, T., and Roh, W.: Improvements in supercooled liquid water simulations of low-level mixed-phase clouds over the Southern Ocean using a single-column model, J. Atmos. Sci., 77, 3803-3819, doi:10.1175/JAS-D-19-0266.1, 2020.

Seiki, T., Roh, W., and Satoh, M.: Cloud microphysics in global cloud resolving models, Atmosphere-Ocean, doi:10.1080/07055900.2022.2075310, 2022.

Sekiguchi, M., and Nakaima, T.: A k-distribution-based radiation code and its computational optimization for an atmospheric general circulation model, J. Quant. Spectrosc. Radiat. Transf., 109, 2779-2793, doi: 10.1016/j.jqsrt.2008.07.013, 2008.

Shi, Y., Zhang, J., Reid, J. S., Hyer, E. J., Eck, T. F., Holben, B. N., and Kahn, R. A.: A critical examination of spatial biases between MODIS and MISR aerosol products – application for potential AERONET deployment, Atmos. Meas. Tech., 4, 2823-2836, doi:10.5194/amt-4-2823-2011, 2011.

Shindell, D. T., Lamarque, J. F., Schulz, M., Flanner, M., Jiao, C., Chin, M., Young, P.J., Lee, Y.H., Rotstayn, L., Mahowald, N., Milly, G., Faluvegi, G., Balkanski, Y., Collins, W.J., Conley, A.J., Dalsoren, S., Easter, R., Ghan, S., Horowitz, L., Liu, X., Myhre, G., Nagashima, T., Naik, V., Rumbold, S.T., Skeie, R., Sudo, K., Szopa, S., Takemura, T., Voulgarakis, A., Yoon, J.H., and Lo, F.: Radiative forcing in the ACCMIP historical and future climate simulations. Atmos. Chem. Phys., 13:2939–2974, 2013.

Sogacheva, L., Popp, T., Sayer, A. M., Dubovik, O., Garay, M. J., Heckel, A., Hsu, N. C., Jethva H., Kahn, R. A., Kolmonen, P., Kosmale, M., de Leeuw, G., Levy, R. C., Litvinov, P., Lyapustin, A., North, P., Torres, O., and Arola, A.: Merging regional and global aerosol optical depth records from major available satellite products, Atmos. Chem. Phys., 20, 2031-2056, https://doi/org/105194/acp-20-2031-2020. 2020.

Sreekanth, V., and Kulkarni, P.: Comparison of V4 and V3 CALIOP (L3) aerosol products: A global perspective, Remote Sensing Applications: Society and Environment 20, 100412, https://doi.org/10.1016/j.rsase.2020.100412, 2020.

Stevens, B., Satoh, M., Auger, L., Biercamp, J., Bretherton, C. S., Chen, X., Düben, P., Judt, F., Khairoutdinov, M., Klocke, D., Kodama, C., Kornblueh L., Lin, S. -J., Neumann, P., Putman, W. M., Röber, N., Shibuya, R., Vanniere, B., Vidale, P. L., Wedi, N., and Zhou, L.: DYAMOND: the Dynamics of the Atmospheric general circulation Modeled On Non-hydrostatic Domains, Prog. Earth. Plan. Sci., 6:61, doi:10.1186/s40645-019-0304-z, 2019.

Stevens, B., Acquistapace, C., Hansen, A., Heinze, R., Klinger, C., Klocke, D., Rybka, H., Schubotz, W., Windmiller, J., Adamidis, P., and Arka, I.: The added value of large-eddy and storm-resolving models for simulating clouds and precipitation, J. Meteorol. Soc. Japan., 98(2), 395-435, doi:10.2151/jmsj.2020-021, 2020.

Sudo, K., Takahashi, M., Kurokawa, J., and Akimoto, H.: CHASER: A global chemical model of the troposphere: 1. Model description, J. Geophys. Res., 107 (D17), 4339, doi:10.1029/2001JD001113, 2002.

Suzuki, K., Nakajima, T., Satoh, M., Tomita, H., Takemura, T., Nakajima, T. Y., and Stephens, G. L.: Global cloud-system-resolving simulation of aerosol effect on warm clouds. Geophys. Res. Lett., 35, L19817. Doi:10.1029/2008GL035449, 2008.

Szopa, S., Naik, V., Adhikary, B., Artaxo, P., Berntsen, T., Collins, W.D., Fuzzi, S., Gallardo, L., Kiendler-Scharr, A., Klimont, Z., Liao, H., Unger, N., and Zanis, P.: Short-Lived Climate Forcers. In Climate Change 2021: The Physical Science Basis. Contribution of Working Group I to the Sixth Assessment Report of the Intergovernmental Panel on Climate Change [Masson-Delmotte, V., Zhai, P., Pirani, A., Connors, S.L., Péan, C., Berger, S., Caud, N., Chen, Y., Goldfarb, L., Gomis, M.I., Huang, M., Leitzell, K., Lonnoy, E., Matthews, J.B.R., Maycock, T.K., Waterfield, T., YelekçI, O., Yu, R., and Zhou, B. (eds.)]. Cambridge University Press, Cambridge, United Kingdom and New York, NY, USA, pp. 817–922, doi:10.1017/9781009157896.008, 2021.

Takata, K., Emori, S., and Watanabe, T.: Development of the minimal advanced treatments of surface interaction and runoff, Global. Planet. Change, 38, 209-222, doi: 10.1016/S0921-8181(03)00030-4, 2003.

Takemura, T., Okamoto, H., Maruyama, Y., Numaguti, A., Higurashi, A., and Nakajima, T.: Global three-dimensional simulation of aerosol optical thickness distribution of various origins, J. Geophys. Res., 105, 17853–17873, doi: 10.1029/2000JD900265, 2000.

Takemura, T., Nozawa, T., Emori, S., Nakajima, T. Y., and Nakajima, T.: Simulation of climate response to aerosol direct and indirect effects with aerosol transport-radiation model. J. Geophys. Res., 110, D02202. https://doi.org/10.1029/2004JD005029, 2005.

Takemura, T., Egashira, M., Matsuzawa, K., Ichijo, H., O'ishi, R., and Abe-Ouchi, A.: A simulation of the global distribution and radiative forcing of soil dust aerosols at the Last Glacial Maximum, Atmos. Chem. Phys., 9, 3061-3073, 2009.

Tatebe, H., Ogura, T., Nitta, T., Komuro, Y., Ogochi, K., Takemura, T., Sudo, K., Sekiguchi, M., Abe, M., Saito, F., Chikira, M., Watanabe, S., Mori, M., Hirota, N., Kawatani, Y., Mochizuki, T., Yoshimura, K., Takata, K., O'ishi, R., Yamazaki, D., Suzuki, T., Kurogi, M., Kataoka, T., Watanabe, M., and Kimoto, M.: Description and basic evaluation of simulated mean state, internal variability, and climate sensitivity in MIROC6. Geosci. Model. Dev. 12:2727–2765. https://doi.org/10.5194/gmd-12-2727-2019, 2019.

Textor, C., Schulz, M., Guibert, S., Kinne, S., Balkanski, Y., Bauer, S., Berntsen, T., Berglen, T., Boucher, O., Chin, M., Dentener, F., Diehl, T., Easter, R., Feichter, J., Fillmore, D., Ghan, S., Ginoux, P., Gong, S., Grini, A., Hendricks, J., Horowitz, L., Huang, P., Isaksen, I., Iversen, T., Kloster, S., Koch, D., Kirkevåg, A., Kristjansson, J. E., Krol, M., Lauer, A., Lamarque, J. F., Liu, X., Montanaro, V., Myhre, G., Penner, J. E., Pitari, G., Reddy, S., Seland, Ø., Stier, P., Takemura, T., and Tie, X.: Analysis and quantification of the diversities of aerosol life cycles within AeroCom, Atmos. Chem. Phys., 6, 1777–1813, doi: 10.5194/acp-6-1777-2006, 2006.

Thorsen, T. J., Winker, D. M., and Ferrare, R. A.: Uncertainty in observational estimates of the aerosol direct radiative effect and forcing, J. Clim., doi:10.1175/JCLI-D-19-1009.1, 2021.

Tomita, H.: New microphysics with five and six categories with diagnostic generation of cloud ice, J. Meteorol. Soc. Jpn., 86A, 121-142, 2008.

Toth, T. D., Zhang, J., Campbell, J. R., Reid, J. S., Shim Y., Johnson, R. S., Smirnov, A., Vaughan, M. A., and Winker, D. M.: Investigating enhanced Aqua MODIS aerosol optical depth retrievals over the mid-to-high latitude Southern Oceans through intercomparison with co-located CALIOP, MAN, and AERONET data sets, J. Geophys. Res. Atmos., 118, 4700-4714, doi:10.1002/jgrd.50311, 2013.

Tsigaridis, K., Daskalakis, N., Kanakidou, M., Adams, P. J., Artaxo, P., Bahadur, R., Balkanski, Y., Bauer, S. E., Bellouin, N., Benedetti, A., Bergman, T., Berntsen, T. K., Beukes, J. P., Bian, H., Carslaw, K. S., Chin, M., Curci, G., Diehl, T., Easter, R. C., Ghan, S. J., Gong, S. L., Hodzic, A., Hoyle, C. R., Iversen, T., Jathar, S., Jimenez, J. L., Kaiser, J. W., Kirkevåg, A., Koch, D., Kokkola, H., Lee, Y. H., Lin, G., Liu, X., Luo, G., Ma, X., Mann, G. W., Mihalopoulos, N., Morcrette, J.-J., Müller, J.-F., Myhre, G., Myriokefalitakis, S., Ng, N. L., O'Donnell, D., Penner, J. E., Pozzoli, L., Pringle, K. J.,

1010   Russell, L. M., Schulz, M., Sciare, J., Seland, Ø., Shindell, D. T., Sillman, S., Skeie, R. B., Spracklen, D., Stavrakou, T., Steenrod, S. D., Takemura, T., Tiitta, P., Tilmes, S., Tost, H., van Noije, T., van Zyl, P. G., von Salzen, K., Yu, F., Wang, Z., Wang, Z., Zaveri, R. A., Zhang, H., Zhang, K., Zhang, Q., and Zhang, X.: The AeroCom evaluation and intercomparison of organic aerosol in global models, Atmos. Chem. Phys., 14, 10845-10895, doi:10.5194/acp-14-10845-2014, 2014.

1015   Twomey, S.: Pollution and the planetary albedo, Atmos. Environ., 8(12), 1251-1256, https://doi.org/10.1016/0004-6981(74)90004-3, 1974.

        van der Werf, Randerson, J. T., Giglio, L., van Leeuwen, T. T., Chen, Y., Rogers, B. M., Mu, M., van Marle, M. J. E., Morton, D. C., Collatz, G. J., Yokelson, R. J., and Kasibhatla, P. S.: Global fire emissions estimates during 1997-2016, Earth Syst. Sci. Data, 9, 697-720, doi:10.5194/essd-9-697-2017, 2017.

1020   Vergara-Temprado, J., Ban, N., Panosetti, D., Schulemmer, L., Schär, C.: Climate models permit convection at much coarser resolutions than previously considered, J. Clim., 33, 1915-1933, doi:10.1175/JCLI-D-19-0286.1, 2020.

        Watson-Parris, D., Schutgems, N. Winker, D., Burton, S. P., Ferrare, R. A., and Stier, P.: On the limits of CALIOP for constraining modeled free tropospheric aerosol. Geophys. Res. Lett., 45, 9260-9266, doi:10.1029/2018GL078195, 2018.

        Wedi, N. P., Polichtchouk, I., Dueben, P., Anantharaj, V. G., Bauer, P., Boussetta, S., Browne, P., Deconinck, W., Gaudin,
1025   W., Hadade, I., Hatfield, S., Iffrig, O., Lopez, P., Maciel, P., Mueller, A., Saarinen, S., Sandu, I., Quintino,T., and Vitart, F.: A baseline for global weather and climate simulations at 1 km resolution, J. Adv. Model. Earth Syst., 12, e2020MS002192. https://doi.org/10.1029/2020MS002192, 2020.

        Wei, J., Peng, Y., Mahmood, R., Sun, L., and Guo, J.: Intercomparison in spatial distributions and temporal trends derived from multi-source satellite aerosol products, Atmos. Chem. Phys., 19, 7183-7207, https://doi.org/10.5194/acp-19-7183-
1030   2019, 2019.

        Winker, D. M., Tackett, J. L., Getzewich, B. J., Liu, Z., Vaughan, M. A., and Rogers, R. R.: The global 3-D distribution of tropospheric aerosols as characterized by CALIOP, Atmos. Chem. Phys., 13, 3345–3361, https://doi.org/10.5194/acp-13- 3345-2013, 2013.

        Zhang, X. Y., Wang, Y. Q., Niu, T., Zhang, X. C., Gong, S. L., Zhang, Y. M., and Sun, J. Y.: Atmospheric aerosol compositions
1035   in China: spatial/temporal variability, chemical signature, regional haze distribution and comparisons with global aerosols, Atmos. Chem. Phys., 12, 779-799, doi:10.5194/acp-12-779-2012, 2012.

Table 1: Experimental design in this study and Goto et al. (2020) as a reference

Name	Version	Resolution [km]	Lev.	Cloud microphysics module	Autoconversion	Reference
NDW6	19	14	78	NDW6	Seifert and Beheng (2006)	This study
NSW6	19	14	78	NSW6	Khairoutdinov and Kogan (2000)	This study
HRM	16	14	38	NSW6	Berry (1967)	Goto et al. (2020)
LRM	16	56	38	NSW6	Berry (1967)	Goto et al. (2020)

1040

Geoscientific
Model Development
Discussions

Table 2: Annual, January and July mean values of clouds, precipitation, and radiation

	Precipitation [mm day^{-1}]	LWP[*1] [g m^{-2}]	COT[*2]	Low-level CF	OSR [W m^{-2}]	SWCRF [W m^{-2}]	OLR [W m^{-2}]	LWCRF [W m^{-2}]
Annual mean								
NDW6	3.01	95.8	7.1	0.19	98.6	-42.5	242.2	21.5
NSW6	2.78	104.4	8.3	0.19	102.0	-45.9	236.8	26.8
Observation[*3]	2.68	119.6	12.9	0.26	99.0	-45.7	240.2	27.9
January								
NDW6	2.99	98.0	7.2	0.18	105.9	-48.4	238.5	22.0
NSW6	2.79	99.1	8.1	0.18	106.7	-49.3	233.4	26.7
Observation[*3]	2.73	120.2	14.5	0.25	105.9	-50.4	237.6	27.6
July								
NDW6	3.09	100.7	7.3	0.21	94.4	-41.8	245.5	21.7
NSW6	2.85	119.0	9.3	0.21	101.6	-48.7	240.4	26.8
Observation[*3]	2.71	121.8	13.2	0.27	94.1	-44.5	244.0	27.7

[*1] LWP over oceans (60°S-60°N); [*2] COT (60°S-60°N); [*3] GPCP (precipitation), MAC (LWP), MODIS (COT), ISCCP (low-level CF), and CERES (OSR, SWCRF, OLR, and LWCRF)

1045 **Table 3: Global and regional averages of the differences in AOT, LWP and shortwave ERFaci between the preindustrial and the present day**

	AOT		LWP		ERFaci	
	NDW6	NSW6	NDW6	NSW6	NDW6	NSW6
Global	0.023	0.031	2.12	0.65	-1.34	-0.63
US[1]	0.071	0.076	7.52	4.96	-4.30	-3.07
Europe[2]	0.062	0.070	15.45	2.52	-7.29	-3.05
East Asia [3]	0.201	0.203	8.77	0.00	-4.92	-3.35
India[4]	0.129	0.176	3.36	-0.44	-2.25	-1.38

[1] US (90°W-60°W, 30°N-50°N); [2] Europe (0°E-30°E, 40°N-60°N) ; [3] East Asia (110°E-140°E, 20°N-50°N) ; [4] India (70°E-90°E, 10°N-35°N)

1050
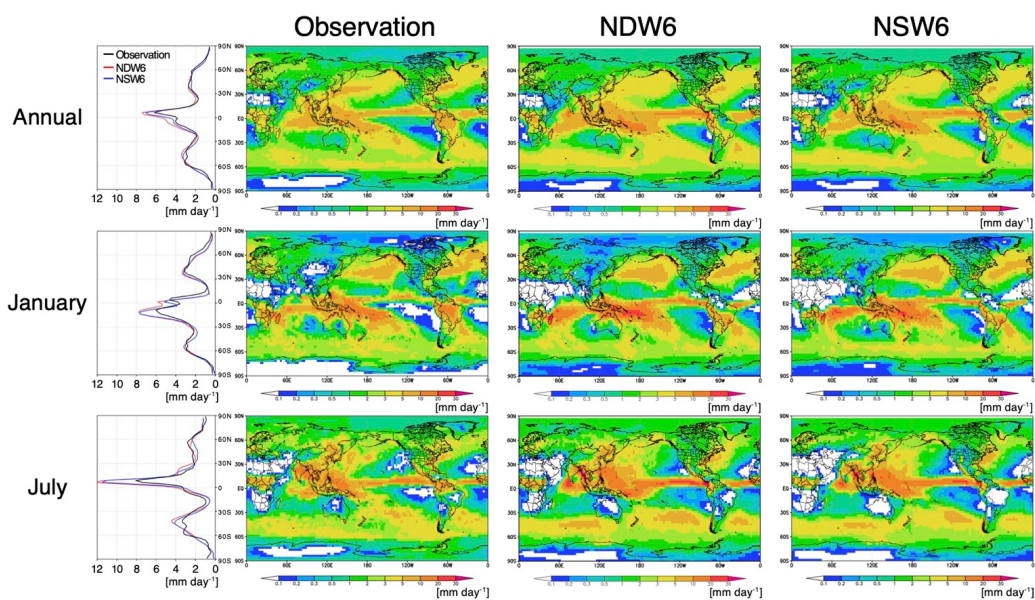
Figure 1: Zonal and horizontal distribution of precipitation (NDW6 and NSW6 defined in Table 1 and GPCP) observations as annual, January, and July averages. All units are in mm day^{-1}.

1055
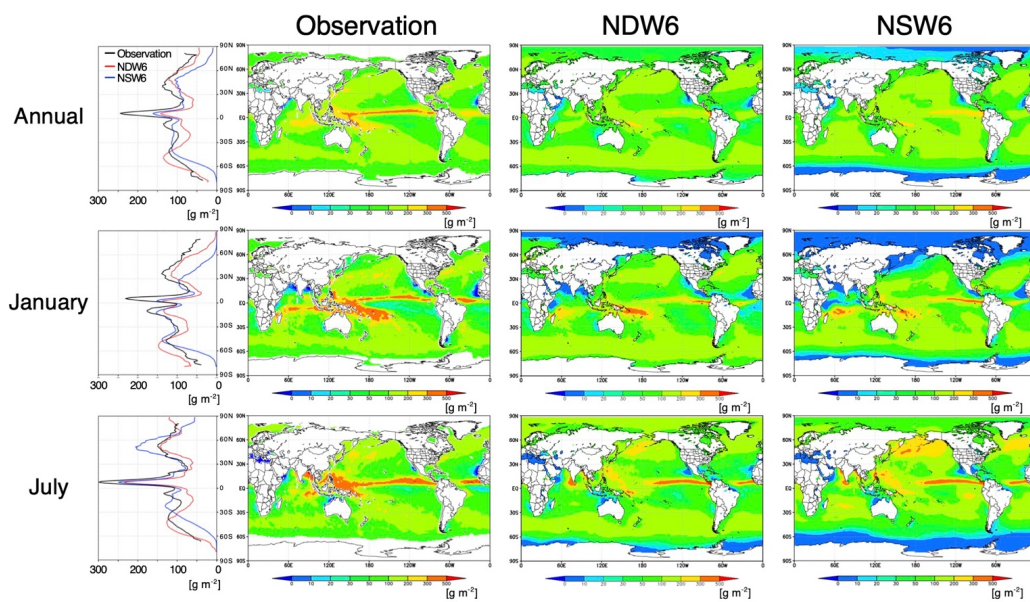
1060 **Figure 2: Zonal and horizontal distributions of LWP (NDW6 and NSW6 defined in Table 1 and MAC as observations) over only the ocean as annual, January, and July averages. All units are in g m⁻².**
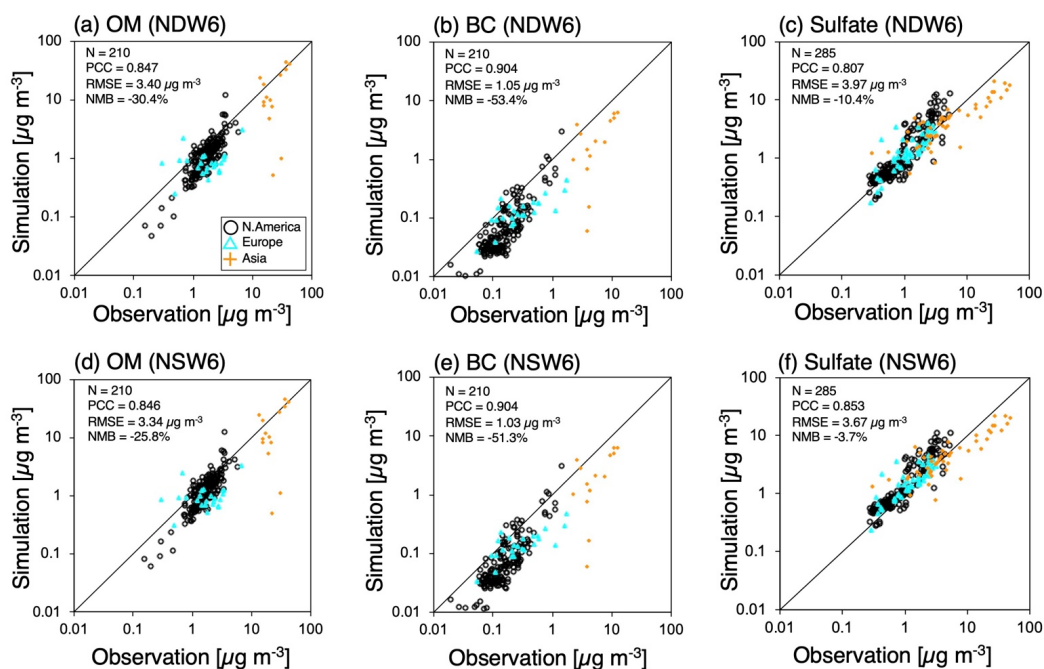
Figure 3: Scatterplots of the annual averages of surface aerosol mass concentrations (OM, BC, and sulfate) between in situ measurements (IMPROVE, EMEP, EANET and CAWNET) and the NICAM simulations (NDW6 and NSW6 defined in Table 1). All units are in µg m⁻³. The statistical metrics (N: sampling number, PCC: Pearson correlation coefficient, RMSE: root-mean-square error, and NMB: normalized mean bias), defined as (A1)-(A3) in Appendix A, are also shown in each panel.

1065

1070
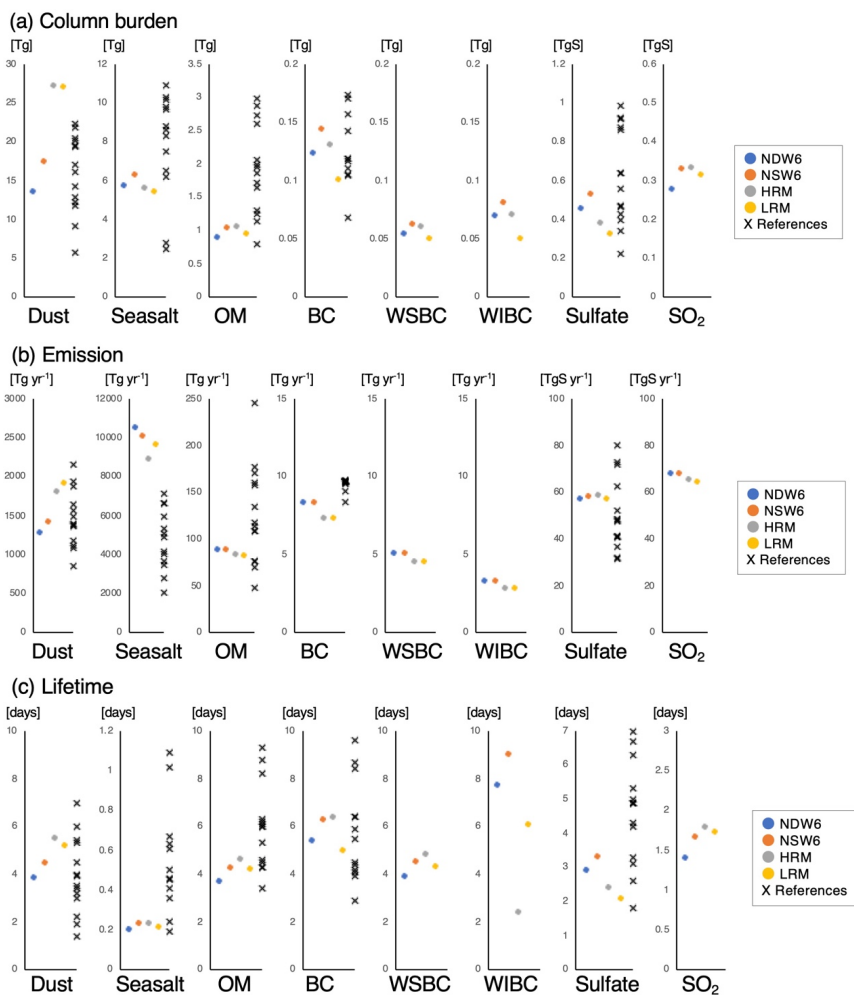
Figure 4: Global and annual mean values of (a) column burdens [Tg or TgS], (b) emission fluxes [Tg yr⁻¹ or TgS yr⁻¹], and (c) atmospheric lifetimes of the simulated aerosols and SO₂ [days]. The NICAM results include NDW6 and NSW6 in this study and HRM and LRM in Goto et al. (2020). The values are also listed in Table A1.
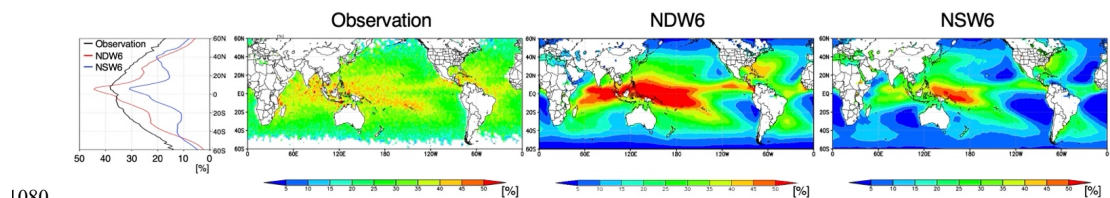
Figure 5: (a) NDW6-simulated, (b) NSW6-simulated, and (c) Cloudsat-retrieved ratio of column precipitation to the sum of column precipitation and total cloud water (RPCW) above 1 km height as annual averages. All units are in %.
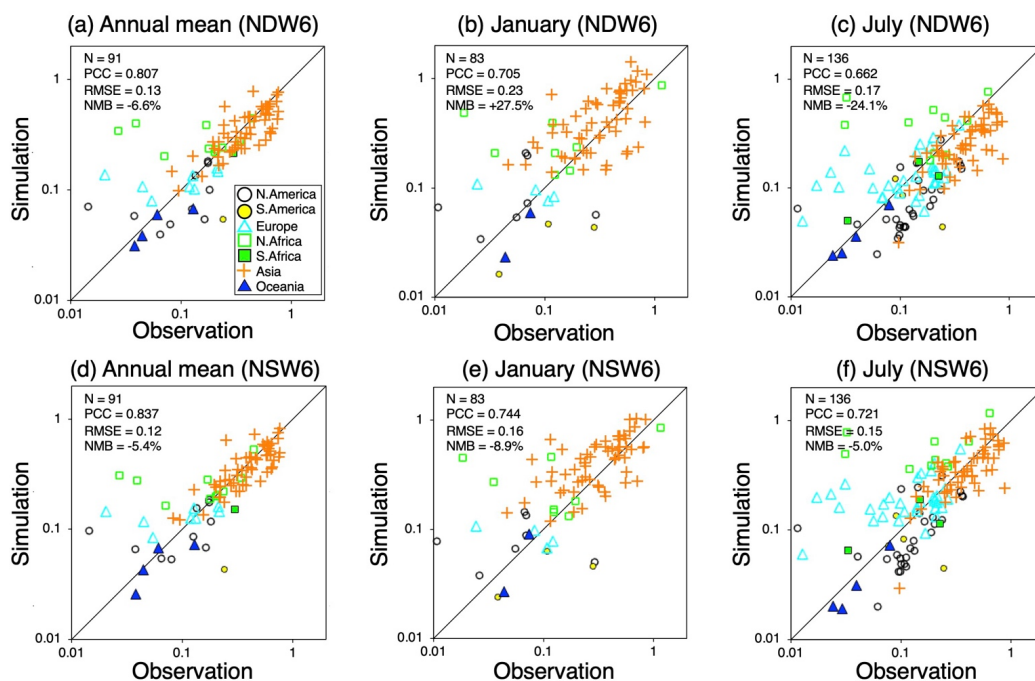
Figure 6: Scatterplot of the annual, January and July averages of AOT between ground-based measurements (AERONET, SKYNET and CARSNET) and the NICAM (NDW6 and NSW6) simulations. The different colors and symbols reflect the sites in the different regions (North America, South America, Europe, North Africa, South Africa, Asia, and Oceania) as defined in panel (a). The numbers located in the upper-left corner in each panel represent the statistical metrics, N, PCC, RMSE and NMB, which are defined as (A1)-(A3) in Appendix A.

1090
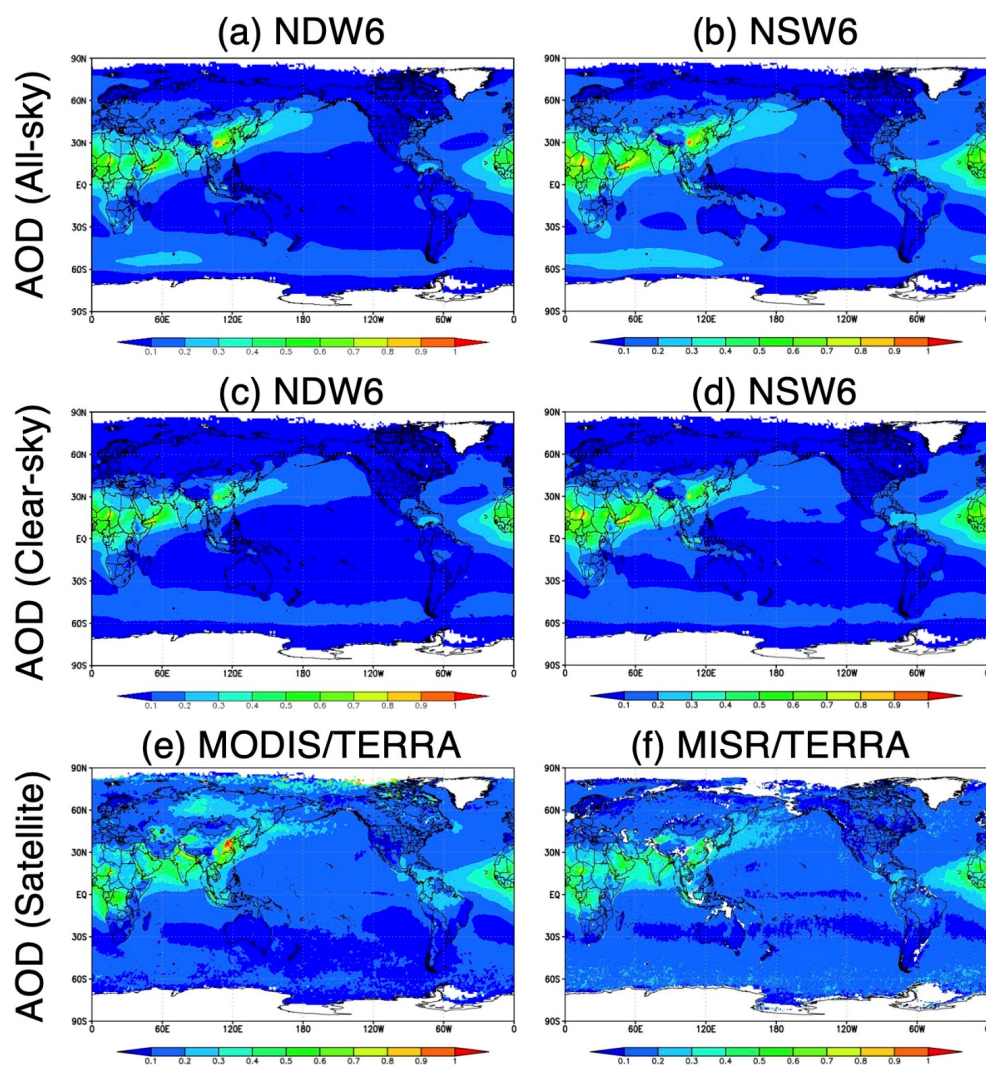
Figure 7: Global distributions of the annual averages of the NDW6-simulated AOT under (a) all-sky and (c) clear-sky conditions, the NSW6-simulated AOT under (b) all-sky and (d) clear-sky conditions, and (e) the MODIS/TERRA-retrieved and (f) the MISR/TERRA-retrieved AOT under clear-sky conditions.
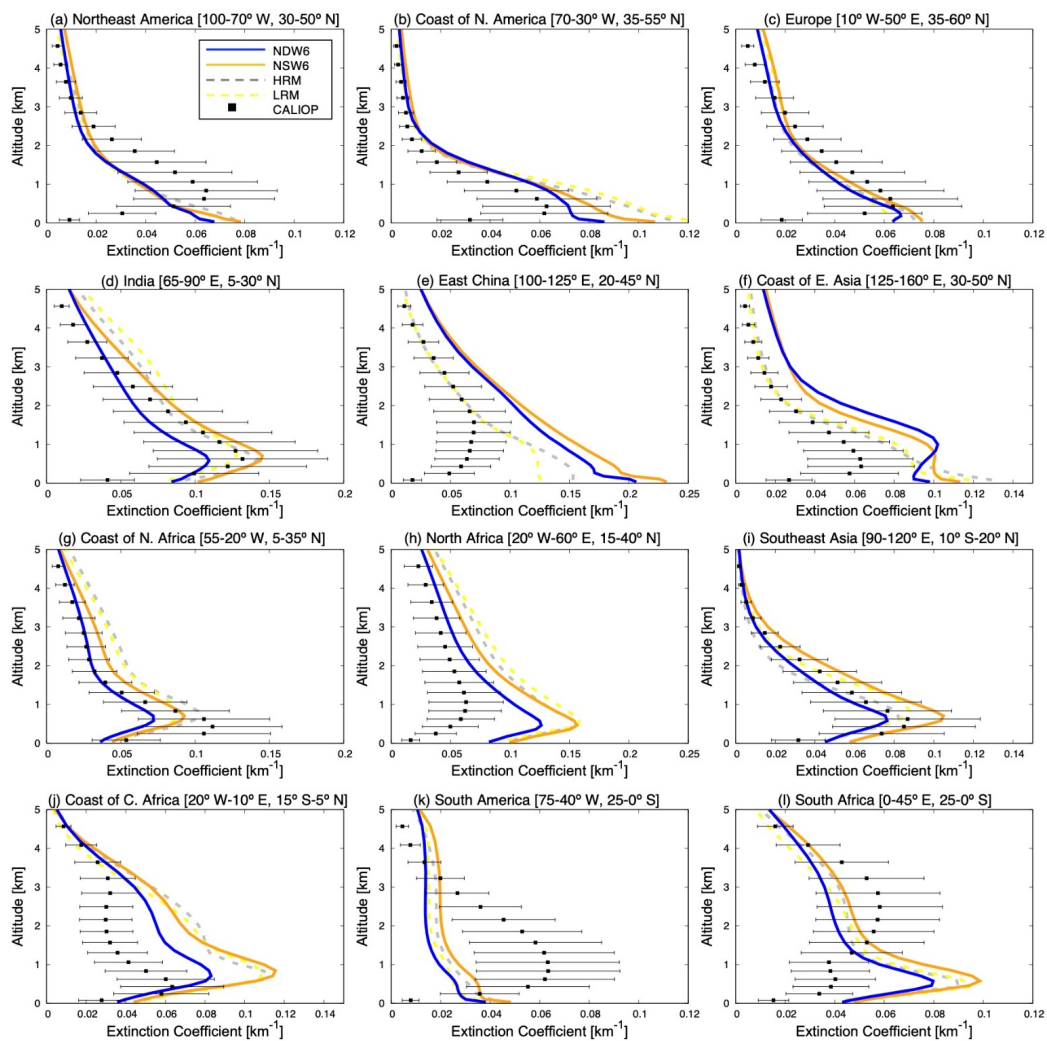
Figure 8: Vertical profiles of the annually and regionally averaged aerosol extinction coefficients from the NICAM simulations (NDW6, NSW6, HRM and LRM) and from CALIOP/CALIPSO observations in 12 different regions, which are generally defined in Goto et al. (2020) and Koffi et al. (2016). The CALIOP-retrieved values include the standard deviation of the results from 2014-2016 as bars. All units are in km^{-1}.
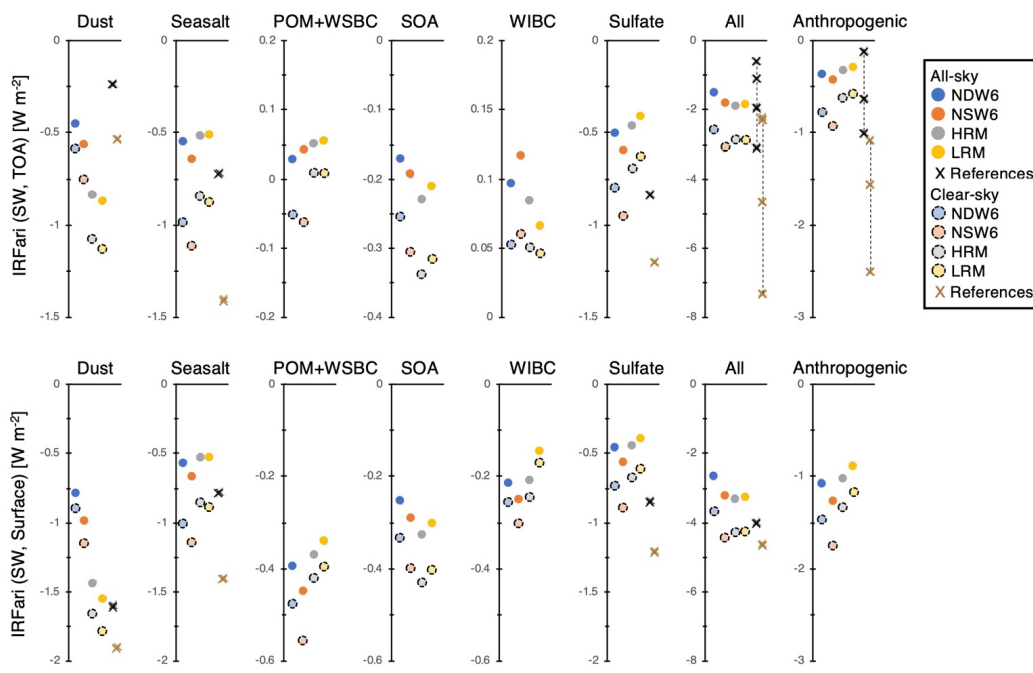
l105

Figure 9: Instantaneous radiative forcing due to aerosol-radiation interaction (IRFari) for each aerosol (dust, sea salt, POM+WSBC, SOA, WIBC, and sulfate), total aerosols (all), and anthropogenic aerosols only (anthropogenic) for shortwave radiation at the TOA. The references are Thorsen et al. (2021) and Kinne (2019). All units are in W m⁻².

1110
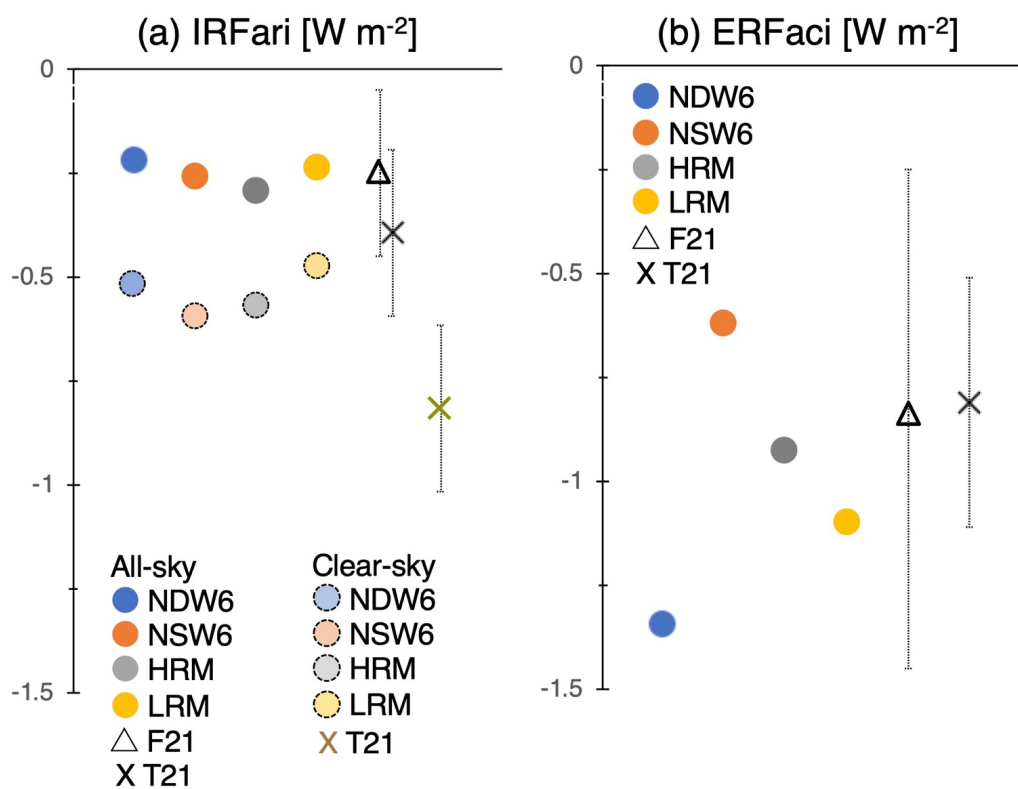
**Figure 10: Global and annual mean values of (a) instantaneous radiative forcing for anthropogenic aerosol-radiation interaction (IRFari) for shortwave radiation at the TOA and (b) effective radiative forcing for anthropogenic aerosol-cloud interaction (ERFaci).**

1115　**Both units are in W m⁻². The references of F21 and T21 are Forster et al. (2021) and Thorsen et al. (2021), respectively.**
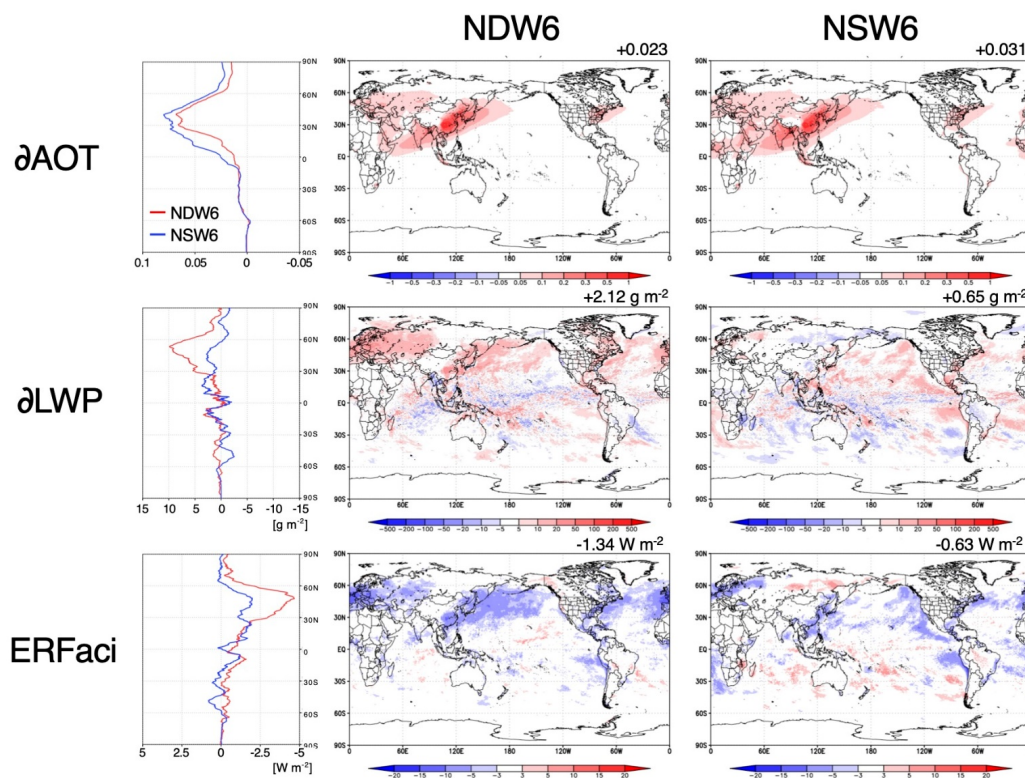
Figure 11: Global distributions of the annual averages of the NDW6- and NSW6-simulated AOT change (∂AOT), LWP change
(∂LWP), and shortwave ERFaci between the present and the preindustrial era. The number located in the upper right in each panel
represents the global and annual mean value.

Geoscientific
Model Development
Discussions

Table A1: Globally and annually mean values of the NICAM-simulated aerosol budgets.

Species	Parameters [Units]	This study (NDW6)	This study (NSW6)	Goto et al. (2020) (HRM)	Goto et al. (2020) (LRM)	References
Dust	Column [Tg]	13.44	17.35	27.08	27.01	16.6 (5.7-22.3)[a]
	Emission [Tg yr^{-1}]	1273	1414	1805	1911	1440 (848-5659)[a]
	Dry Deposition [Tg yr^{-1}]	234	289	342	363	396 (37-2791)[b]
	Grav. Deposition [Tg yr^{-1}]	380	452	634	663	314 (22-2475)[b]
	Wet Deposition [Tg yr^{-1}]	669	689	825	880	357 (295-1382)[b]
	Lifetime [Day]	3.82	4.43	5.49	5.17	3.7 (1.4-7.0)[a]
Seasalt	Column [Tg]	5.69	6.25	5.60	5.42	8.7 (2.5-26.4)[a]
	Emission [Tg yr^{-1}]	10486	10048	8856	9624	4980 (2030-50000)[a]
	Dry Deposition [Tg yr^{-1}]	2820	3006	2272	2169	1313[c]
	Grav. Deposition [Tg yr^{-1}]	2169	2316	1998	1951	327[c]
	Wet Deposition [Tg yr^{-1}]	5498	4726	4586	5504	1889[c]
	Lifetime [Day]	0.20	0.23	0.23	0.21	0.56 (0.19-1.51)[a]
OM	Column [Tg]	0.88	1.02	1.04	0.94	1.91 (0.79-2.99)[a]
	Emission [Tg yr^{-1}][h]	87.2	87.2	82.2	81.9	116.0 (48.0-246.0)[a]
	Dry Deposition [Tg yr^{-1}]	7.0	7.4	6.3	6.6	approximately 15 (0.2-28)[d]
	Grav. Deposition [Tg yr^{-1}]	6.1	6.8	3.7	3.9	
	Wet Deposition [Tg yr^{-1}]	74.3	73.8	72.6	71.4	approximately 90 (approximately 50-140)[d]
	Lifetime [Day]	3.66	4.24	4.60	4.17	6.0 (3.4-9.3)[a]
BC	Column [Tg]	0.12	0.14	0.13	0.1	0.131 (0.068-0.260)[a]
	Emission [Tg yr^{-1}][h]	8.3	8.3	7.3	7.3	9.7 (8.4-9.7)[a]
	Dry Deposition [Tg yr^{-1}]	0.9	1.0	0.8	0.8	
	Grav. Deposition [Tg yr^{-1}]	0.3	0.3	0.2	0.2	
	Wet Deposition [Tg yr^{-1}]	7.1	7.0	6.3	6.3	
	Lifetime [Day]	5.38	6.26	6.37	4.96	5.5 (2.9-8.7)[a]
WSBC	Column [Tg]	0.05	0.06	0.06	0.05	0.19[f]
	Emission [Tg yr^{-1}][i]	5.0	5.0	4.5	4.5	
	Dry Deposition [Tg yr^{-1}]	0.5	0.5	0.4	0.4	
	Grav. Deposition [Tg yr^{-1}]	0.3	0.3	0.2	0.2	
	Wet Deposition [Tg yr^{-1}]	4.3	4.3	3.9	3.9	
	Lifetime [Day]	3.88	4.49	4.78	4.29	6.4[f]
WIBC	Column [Tg]	0.07	0.08	0.07	0.05	0.03[f]

|						
	Emission [Tg yr^{-1}][i]	3.3	3.3	2.8	2.8	
	Dry Deposition [Tg yr^{-1}]	0.5	0.5	0.4	0.4	
	Grav. Deposition [Tg yr^{-1}]	0.0	0.0	0	0	
	Wet Deposition [Tg yr^{-1}]	2.8	2.8	2.4	2.4	
	Lifetime [Day]	7.68	9.00	8.95	6.04	1.0[f], 1.0-1.7[g], 9.6 (w/o aging)[g]
Sulfate	Column [TgS]	0.45	0.52	0.38	0.32	0.60 (0.22-0.98)[a]
	Production [TgS yr^{-1}]	57.1	57.8	58.4	56.7	37.6-61.1[c]
	from the gas phase	13.3	14.6	16.8	16.1	6.2[c] -17.4[e]
	from the aqueous phase	43.7	43.2	41.7	40.6	21.1[e]-58.8[c]
	Dry Deposition [TgS yr^{-1}]	3.8	4.6	3.9	3.6	5.8-7.6[c]
	Grav. Deposition [Tg yr^{-1}]	0.1	0.1	0.5	0.4	0.0[c]
	Wet Deposition [TgS yr^{-1}]	53.4	53.4	52.0	50.4	31.8-53.5[c]
	Lifetime [Day]	2.89	3.29	2.38	2.05	4.9 (1.8-7.0)[a]
SO₂	Column [TgS]	0.28	0.33	0.33	0.31	
	Production [TgS yr^{-1}][h]	67.8	67.5	65.0	64.1	
	Chemical loss (gas phase)	13.3	14.6	13.0	12.5	
	Chemical loss (aqueous phase)	43.7	43.2	41.7	40.6	
	Dry Deposition [TgS yr^{-1}]	13.0	13.2	11.7	12.0	
	Wet Deposition [TgS yr^{-1}]	2.3	1.8	1.4	1.1	
	Lifetime [Day]	1.40	1.66	1.79	1.72	

1125

[a] Gliß et al. (2021); [b] Huneeus et al. (2011); [c] Takemura et al. (2000); [d] Tsigaridis et al. (2014); [e] Goto et al. (2011); [f] Chung and Seinfeld (2002); [g] Goto et al. (2012); [h] The global and annual mean values in this study (NDW6 and NSW6) are slightly different from those (HRM and LRM) in Goto et al. (2020) because the method of remapping from a latitude-longitude grid emission map to an icosahedral grid in NICAM is modified in this study.

1130
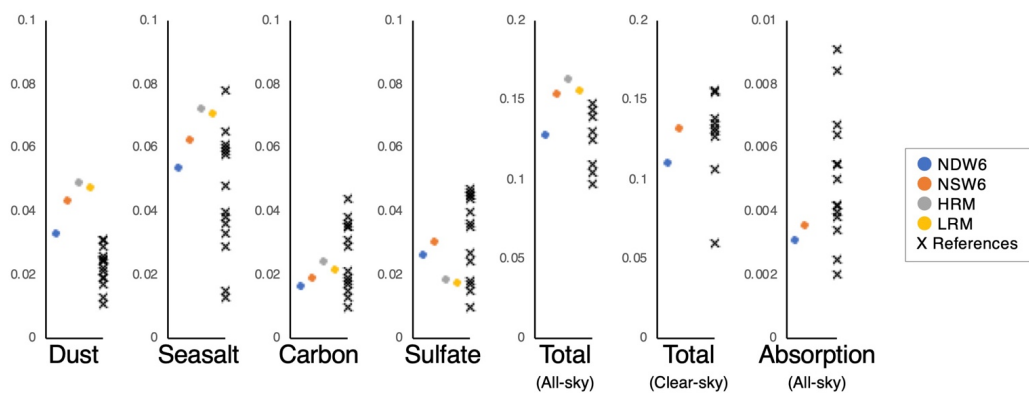
Figure C1: Global and annual mean values of AOT for chemical components (dust, sea salt, carbonaceous aerosols, and sulfate) under all sky conditions, AOT of total aerosols under both all-sky and clear-sky conditions, and absorption AOT under all-sky conditions. There are no HRM and LRM results for AOT under clear-sky conditions and absorption AOT.

1135
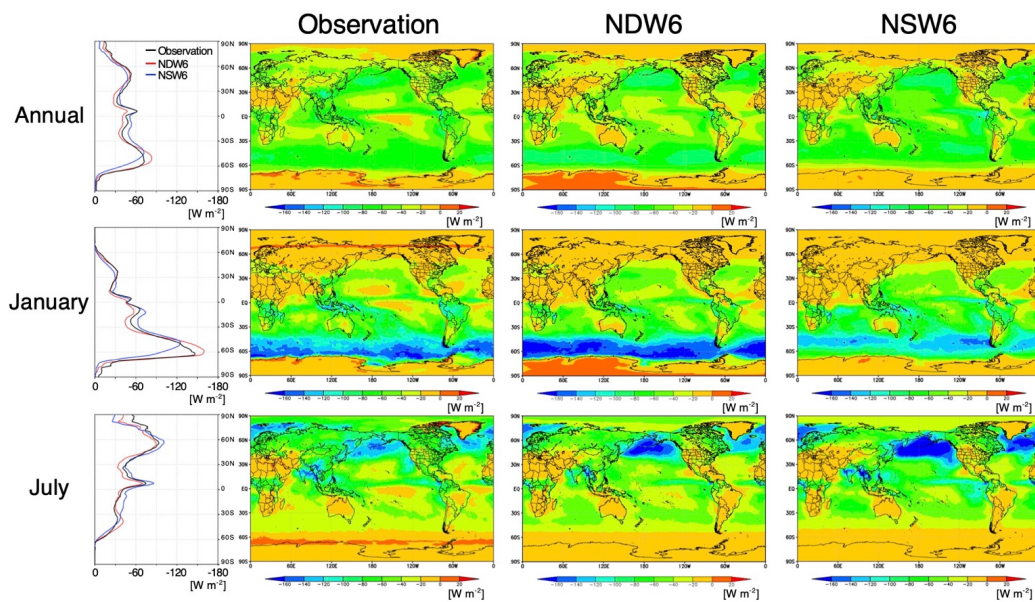
Figure E1: Zonal and horizontal distribution of SWCRF (NDW6 and NSW6 defined in Table 1 anSame as Figure 1 but for SWCRF. The observation is from CERES. All units are in W m⁻².

1140
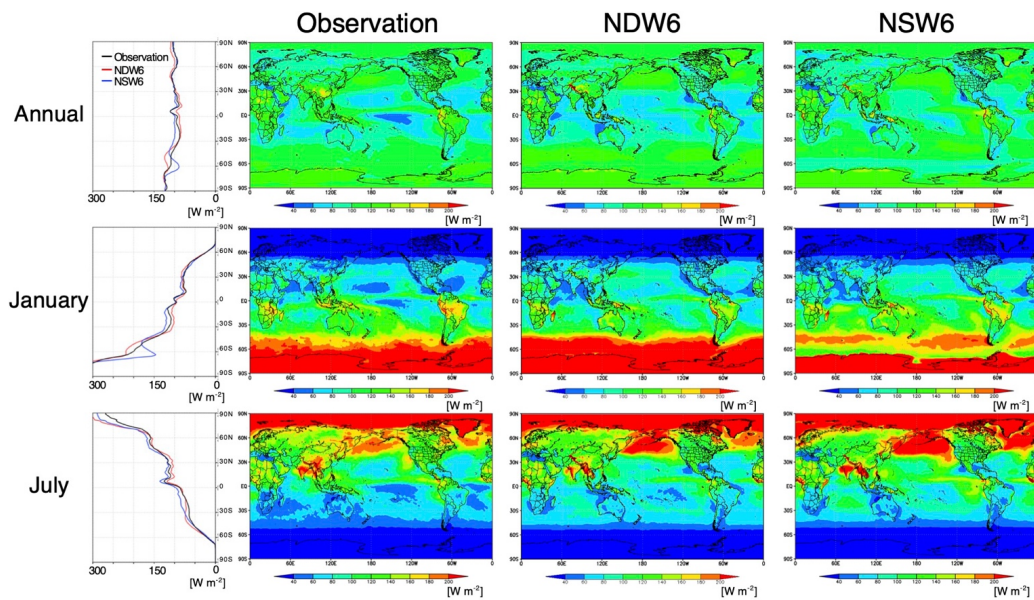
Figure E2: Same as Figure E1 but for OSR.

1145